

East Antarctic Ice Sheet variability during the middle Miocene Climate Transition captured in drill cores from the Friis Hills, Transantarctic Mountains

Hannah Chorley^{1,†}, Richard Levy^{1,2}, Tim Naish¹, Adam Lewis³, Stephen Cox⁴, Sidney Hemming⁴, Christian Ohneiser⁵, Andrew Gorman⁵, Margaret Harper⁶, Aline Homes⁶, Jenni Hopkins⁶, Joe Prebble², Marjolaine Verret¹, Warren Dickinson¹, Fabio Florindo⁷, Nicholas Golledge¹, Anna Ruth Halberstadt⁸, Douglas Kowalewski⁹, Robert McKay¹, Stephen Meyers¹⁰, Jacob Anderson¹¹, Bob Dagg⁵, and Pontus Lurcock⁷

¹Antarctic Research Centre, Victoria University of Wellington, Wellington 6012, New Zealand

²GNS Science, Lower Hutt 5010, New Zealand

³Department of Geosciences, North Dakota State University, Fargo, North Dakota 58105, USA

⁴Lamont-Doherty Earth Observatory, Columbia University, Palisades, New York 10964, USA

⁵Department of Geology, University of Otago, Dunedin 9054, New Zealand

⁶School of Geography, Earth and Environmental Science, Victoria University of Wellington, Wellington 6012, New Zealand

⁷Istituto Nazionale di Geofisica e Vulcanologia, Rome 00143, Italy

⁸Berkeley Geochronology Center, 2455 Ridge Road, Berkeley, California 94709, USA

⁹Earth Environment and Physics, Worcester State University, Worcester, Massachusetts 01602, USA

¹⁰Department of Geoscience, University of Wisconsin–Madison, Madison, Wisconsin 53706, USA

¹¹Department of Marine Science, University of Otago, Dunedin 9054, New Zealand

ABSTRACT

This study describes 16 well-dated, terrestrial glacial sedimentary cycles deposited during astronomically paced climate cycles from the termination of the Miocene Climatic Optimum (MCO) through the middle Miocene Climate Transition (MMCT) (15.1–13.8 Ma) in the Friis Hills, Transantarctic Mountains, Antarctica. Three locations were continuously cored (79% recovery) to a maximum depth of 50.48 m through a succession of interbedded till sheets and fossil-bearing, fluvio-lacustrine sediments. A composite chronostratigraphic framework is presented for the cores based on the previous mapping, a seismic refraction survey that defines basin geometry, and a new, integrated age model based on paleomagnetic stratigraphy that is constrained by radioisotopic $^{40}\text{Ar}/^{39}\text{Ar}$ numeric ages on two newly identified silicic tephra.

The paleoecologic and sedimentologic characteristics of organic-rich lithologies are relatively consistent up-section, which implies that successively younger interglacial deposits during the MMCT represented broadly

similar environmental and climatic conditions. During these interglacials, the Friis Hills hinterland was likely ice-free. Major disconformities in the section suggest a transition to colder climates, and after ca. 14.6 Ma, thicker, more extensive and erosive ice cover occurred across the Friis Hills during glacial episodes. Diamictites in the upper three cycles suggest that climate cooled and became drier after ca. 14.2 Ma. However, cyclical retreat of the ice and a return to warm climate conditions during interglacials continued through ca. 13.9 Ma. These direct records reflect a highly variable East Antarctic Ice Sheet margin but show that the ice margin became progressively more extensive during successive glacial intervals, which is consistent with a cooling trend toward more glacial values in the far-field benthic foraminifera $\delta^{18}\text{O}$ proxy ice volume and temperature record.

Age constraints show that glacial-interglacial variability at the terrestrial margin of the East Antarctic Ice Sheet was primarily paced by astronomical precession (~23 k.y.) through the onset of the MMCT (15–14.7 Ma). Precession-driven cycles are modulated by short-period (~100 k.y.) eccentricity cycles. Intervals of maximum eccentricity (high seasonality) coincide with sedimentary cycles comprising thin diamictites and relatively

thick interglacial sandstone and mudstone units. Intervals of minimum eccentricity (low seasonality) coincide with sedimentary cycles comprising thick diamictites and relatively thin interglacial sedimentary deposits. Major disconformities in the Friis Hills succession that span more than ~100 k.y. reflect episodes of expansion of erosive ice across, and well beyond, the Transantarctic Mountains and coincide with nodes in eccentricity (~400 k.y.). These relationships suggest that during relatively warm intervals in the middle Miocene, the East Antarctic Ice Sheet expanded and contracted over 100 k.y. cycles, while its margins continued to fluctuate at higher (~23 k.y.) frequency. After 14.5 Ma, obliquity is the dominant frequency in $\delta^{18}\text{O}$ records, marking a period during which large regions of the Antarctic Ice Sheet grounded in marine environments.

INTRODUCTION

Ice Sheet Evolution through the Middle Miocene Climate Transition

Short-term variations and longer duration trends in Earth's climate through the Cenozoic are revealed by compilations of high-resolution, deep-sea benthic foraminifera $\delta^{18}\text{O}$ records (De

Hannah Chorley  <https://orcid.org/0000-0002-5239-4748>
[†]hkchorley@gmail.com

Vleeschouwer et al., 2017; Westerhold et al., 2020; Zachos et al., 2001). These records show a general cooling trend since the onset of large, continental-scale glaciation in Antarctica ca. 34 Ma (Coxall et al., 2005; Galeotti et al., 2016; Scher et al., 2011). This long-term climatic transition from a warm and relatively ice-free “greenhouse world” to today, where large ice sheets occupy both poles, was punctuated by geologically short (\sim 1–2 m.y.) intervals of warmth and distinct, relatively rapid, cooling steps. The most recent of these large, warm-to-cold climatic shifts occurred between ca. 15 Ma and 13.8 Ma during the middle Miocene Climate Transition (MMCT) (Flower and Kennett, 1993, 1994; Shevenell et al., 2004).

The MMCT marks the termination of the Miocene Climate Optimum (MCO), a period of warmth spanning ca. 17 Ma to ca. 15 Ma during which Earth’s average surface temperatures at times ranged between 4 °C and 8 °C warmer than pre-industrial (pre-1850 CE) values, and atmospheric CO₂ concentrations occasionally exceeded 600 ppm (Böhme, 2003; Greenop et al., 2014; Herold et al., 2010; Steinthorsdóttir et al., 2021; Utescher et al., 2011; You, 2010; You et al., 2009). The termination of the MCO and onset of the MMCT is reflected in deep-sea δ¹⁸O records by a relatively subtle increase in glacial δ¹⁸O values and a trend toward higher average values beginning at ca. 14.8 Ma (Hobourn et al., 2014; Fig. 1). This shift coincides with a drop in average CO₂ concentrations well below 400 ppm (Fig. 1). The MMCT lasted for approximately 1 m.y. and culminated in a large (\sim 0.4‰), stepped increase in average δ¹⁸O values at 13.8 Ma (Fig. 1). Importantly, this last major step in the MMCT coincides with a drop in atmospheric CO₂ concentration below 300 ppm (Badger et al., 2013; Super et al., 2018; Fig. 1).

It has long been inferred that the East Antarctic Ice Sheet expanded and stabilized during the MMCT and that Antarctica’s terrestrial environments cooled and became arid (Clapperton and Sugden, 1990; Marchant, 1993; Sugden and Denton, 2004; Sugden et al., 1993). These inferences are primarily based on evidence captured in sedimentary deposits and geomorphological features at high elevations (>1000 m) in the Transantarctic Mountains. Of particular importance are 15-m.y.-old ash deposits in the Asgard Range of the McMurdo Dry Valleys (McMurdo Dry Valleys) (Fig. 2) that suggest minimal landscape modification at these high-elevation locations since the end of the MCO (Marchant, 1993).

Major disconformities in offshore drill cores, including the ANDRILL Southern McMurdo Sound Project drill core AND-2A and International Ocean Discovery Program (IODP)

Expedition Site U1531 (Figs. 1–2), occur between 15 Ma and 13 Ma and suggest that the Antarctic Ice Sheet advanced across the Ross Sea during glacial episodes and became progressively more extensive during the later stages of the MMCT (Fielding et al., 2011; Levy et al., 2016, 2022; McKay et al., 2022; Passchier et al., 2011). Geochemical provenance analysis of rock and sediment clasts in cores from IODP Sites U1356 and 1165 indicate that the East Antarctic Ice Sheet margin repeatedly retreated inland across the Wilkes subglacial basin and Lambert Graben and advanced again into marine environments between 14.1 Ma and 13.8 Ma (Pierce et al., 2017; Sangiorgi et al., 2018; Fig. 1). Sea-surface temperatures in the Southern Ocean dropped by 2–6 °C between ca. 14.1 Ma and 13.8 Ma (Leutert et al., 2020; Shevenell et al., 2004; Fig. 1), and sea level fell by 59 ± 6 m at ca. 13.9 Ma (John et al., 2011). These data show that the Antarctic Ice Sheet expanded to the edge of the Antarctic continental shelf during the MMCT and support terrestrial evidence in the Transantarctic Mountains for climatic cooling and significant advance of the ice sheet at this time.

However, a detailed history of Antarctic climate and ice-sheet response through this transition has been missing due to a scarcity of well-dated, relatively continuous terrestrial stratigraphic sequences and incomplete marine records resulting from the erosion of sediments during episodes of glacial expansion. Additional insight into Antarctic environmental evolution through this transition is important as it occurred during a period when CO₂ dropped from >600 ppm to <300 ppm (Badger et al., 2013; Greenop et al., 2014; Fig. 1). Geological data and modeling studies suggest an atmospheric CO₂ concentration of ~400 ppm represents a threshold below which climatic cooling at high southern latitudes enables marine ice sheets and sea ice to expand and persist (Foster and Rohling, 2013; Gasson et al., 2016; Halberstadt et al., 2021; Levy et al., 2016, 2019; Naish et al., 2009). Today, atmospheric CO₂ concentrations are above 400 ppm due to anthropogenic emissions, and future projections show that atmospheric CO₂ concentrations could exceed 600 ppm well before the end of the century if we fail to achieve greenhouse gas emissions reduction targets (IPCC, 2013; Meinshausen et al., 2011; Tebaldi et al., 2021).

These projected increases in CO₂ concentrations represent a reversal of the downward trend that characterized the MMCT. Therefore, well-constrained stratigraphic data from the Antarctic continental margin through the MMCT offers insight into the possible long-term (multi-centennial) environmental response as climate equilibrates under high atmospheric CO₂ concentrations. Here, we present a new, well-dated

record of terrestrial environmental change from the Friis Hills, Transantarctic Mountains, Antarctica. These data augment other geological records from Southern Victoria Land and allow us to examine the terrestrial glacial and climatic response of the region through an episode of significant global climate change.

Early to Middle Miocene Terrestrial Records from the McMurdo Dry Valleys

Terrestrial sedimentary deposits of middle Miocene age in the Ross Embayment are primarily located in the McMurdo Dry Valleys, where today they occur at high elevation (>1000 m) in the Asgard Range (Marchant, 1993), Western Olympus Range (Lewis et al., 2008; Lewis et al., 2007), and Friis Hills (Lewis and Ashworth, 2016; Fig. 2C). Most of these sedimentary records are composed of tills, fluvial lacustrine sequences, and colluvium, and the majority post-date the MCO (Fig. 1). Key deposits in the Asgard Range include the Sessrummir and Asgard tills (Marchant, 1993). Sediments deposited in the Olympus Range during the MMCT include Circe till, Electra colluvium, Dido drift (Lewis et al., 2007), and fossil-rich, moraine-dammed, glacial-lacustrine deposits near Mount Boreas (Lewis et al., 2008) (Figs. 1–2). Distinctive geomorphological features, including a network of bedrock channels and scoured terrain that characterize the Labyrinth and correlative surfaces (Lewis et al., 2006), also offer insights into the history of ice-sheet development in the McMurdo Dry Valleys.

The most complete succession of middle Miocene terrestrial sediments in the Transantarctic Mountains is preserved in the Friis Hills (Lewis and Ashworth, 2016). The Friis Hills (77°45'S, 161°30'E) are located at the head of the Taylor Valley in the McMurdo Dry Valleys and comprise an inselberg that projects up to 1100 m above the surrounding topographic features (Fig. 2D). A glacially molded surface that forms the top of the inselberg extends 8 km east to west and 4 km north to south. The surface includes three rounded dolerite hills that rise 150–250 m above the main surface (Fig. 2D) and bound three sectors to include a small bench to the west, a central valley that slopes to the SE at an orientation of 135° and opens to the south, and a broad bench to the east (Fig. 2D). The surface has an average elevation of 1325 m above sea level, which is similar to a bedrock platform on Solitary Rocks, 4 km to the south, and to benches in the Asgard Range (Lewis and Ashworth, 2016) that contain the Sessrummir and Asgard tills and other middle Miocene sediments (Marchant, 1993).

The Friis Hills sediments comprise a sequence of glacial, glacio-fluvial, and glacio-lacustrine sediments that are classified into three

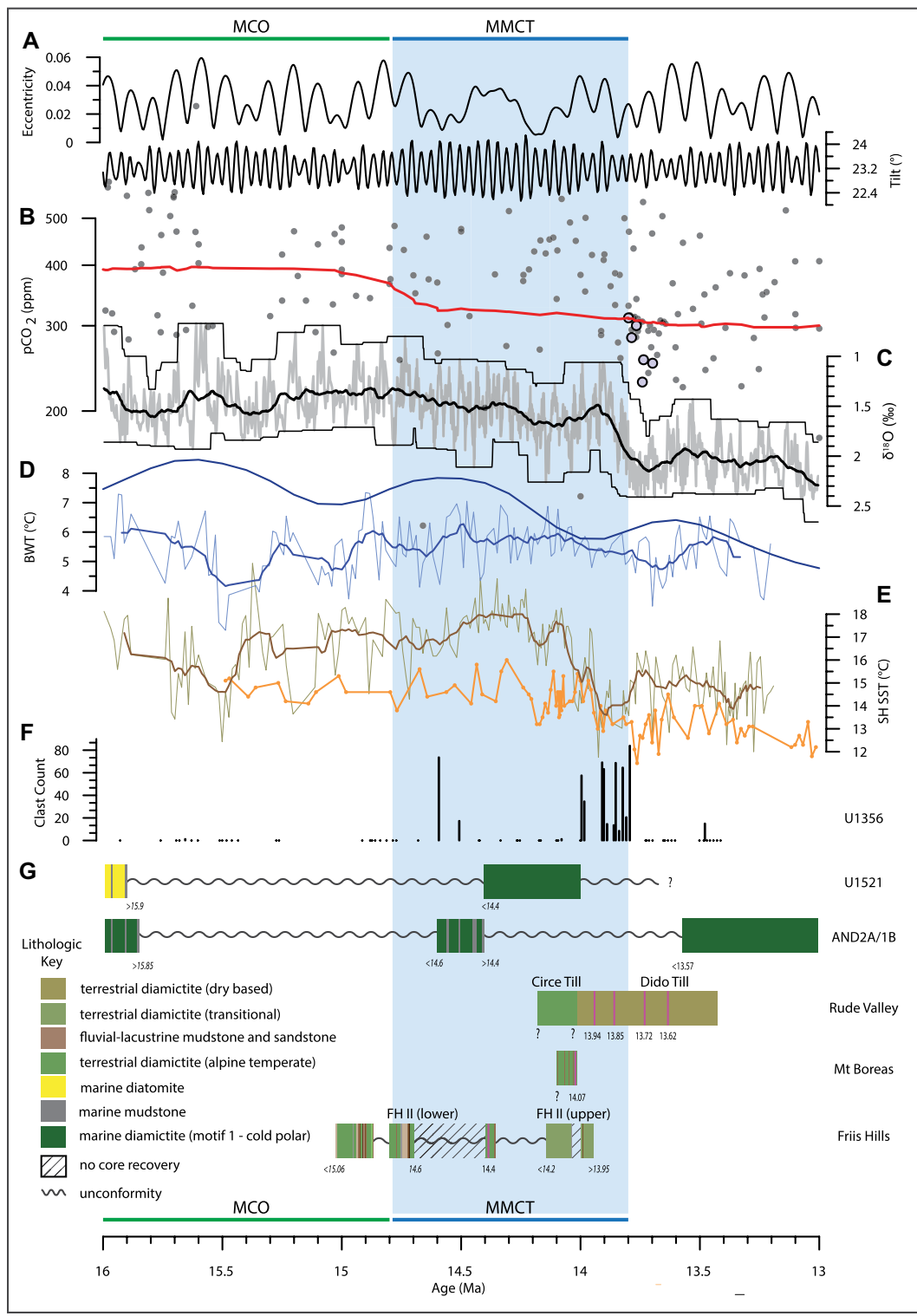


Figure 1. Summary of major climate drivers (astronomical cycles and atmospheric CO₂), proxy environmental records from the deep ocean, and key geological records from the Antarctic margin spanning the middle Miocene including the Miocene Climatic Optimum (MCO) and middle Miocene Climate Transition (MMCT).

(A) Short-period (100 k.y.) eccentricity and axial tilt (obliquity) after Laskar (2011). (B) Atmospheric CO₂ compilation comprises data from a range of proxies, including boron isotopes (Foster et al., 2012; Greenop et al., 2014; Raitzsch et al., 2021; Sosdian et al., 2018), B/Ca (Badger et al., 2013), phytoplankton/alkenones (Badger et al., 2013; Bolton et al., 2016; Super et al., 2018; Zhang et al., 2013), leaf stomata (Beerling et al., 2009; Kürschner et al., 2008), paleosols (Cerling, 1992; Ekart et al., 1999; Ji et al., 2018; Retallack, 2009), and phytanes (Witkowski et al., 2018). Solid red line displays a 2 m.y. moving average. (C) Splice of deep-sea benthic foraminifera δ¹⁸O data (light gray) reflect changes in ice volume and deep/bottom water temperature (De Vleeschouwer et al., 2017). Solid black line displays a 150 k.y. moving average. Maximum and minimum values are determined within each 150 k.y. window and create the envelope (black lines) that bounds the δ¹⁸O data. (D) Bottom-water temperature (BWT) data from ODP Site 1171 (southwest Tasman Sea: 48.4999°S, 146.1115°E) (Shevenell et al., 2008) (blue), which were derived from the compilation of Cramer et al. (2011) using their Equation 7a (dark blue). Solid line through

data from ODP Site 1171 displays a 9 point running average. (E) Sea-surface temperature (SST) data for the Southern Hemisphere (SH) from ODP Site 1171 using the Mg/Ca proxy (Shevenell et al., 2004) (olive green; brown line is 9 pt running average) and the TEX₈₆ proxy (orange) (Leutert et al., 2020) using the calibration of (Ho and Laepple, 2016). (F) Sedimentary clast count data from IODP Site U1356 (Sangiorgi et al., 2018). (G) Summary of stratigraphic records from the central Ross Sea, McMurdo Sound, and Transantarctic Mountains discussed in this paper. Numbers indicate key age datums based on biostratigraphy and/or paleomagnetic reversals (italics) and tephra. AND—Antarctic Drilling Project; BWT—Bottom Water Temperature; FH—Friis Hills.

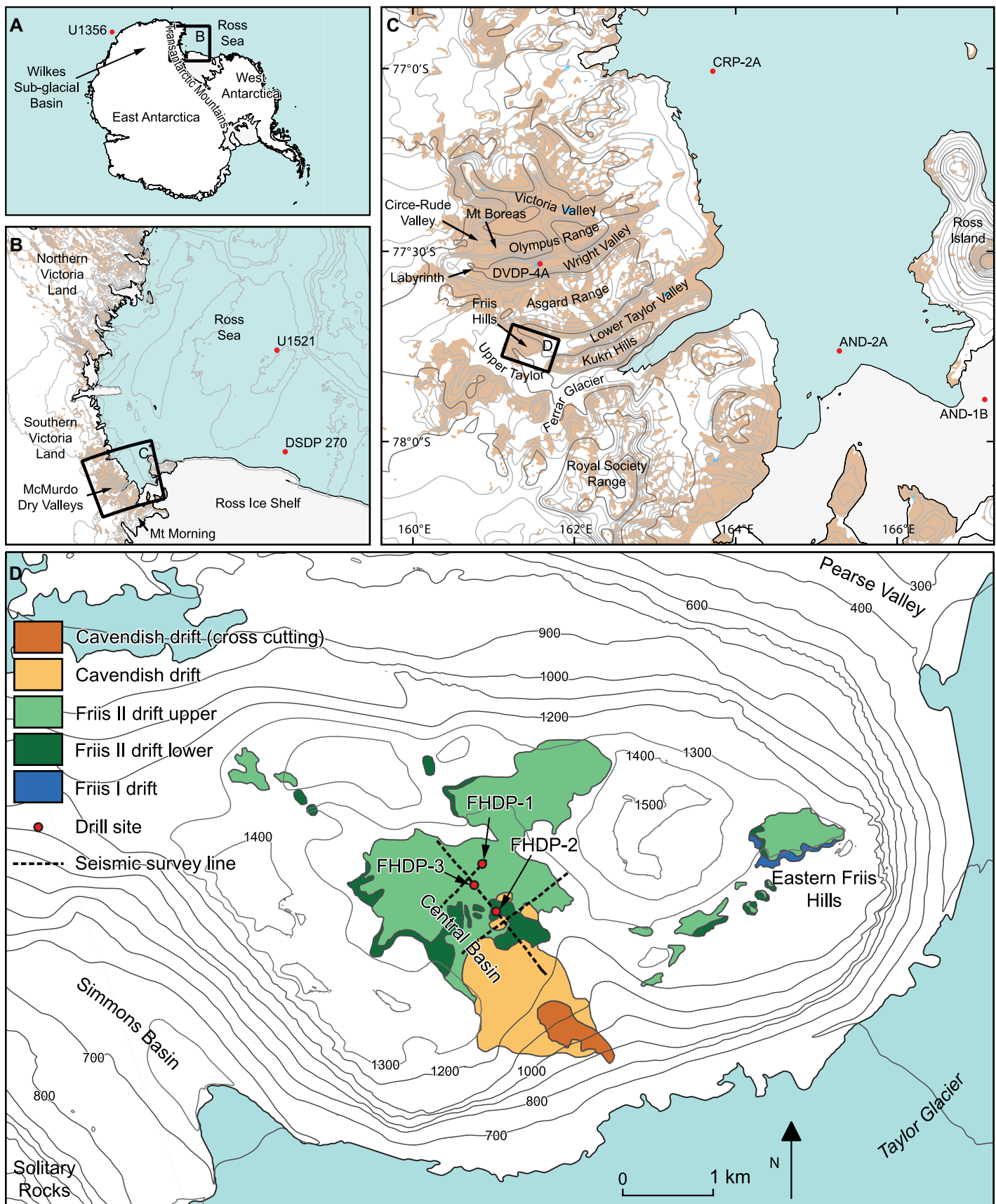


Figure 2. Maps show locations of drill sites (red dots) and other middle Miocene records and regional features discussed in this paper. (A) Antarctica, including International Ocean Discovery Program (IODP) Site 1356. (B) Central and western Ross Sea Region. (C) Southern Victoria Land, McMurdo Sound, and the McMurdo Dry Valleys including IODP Site U1521. (D) Friis Hills with outcrop map from Lewis and Ashworth (2016). Dashed lines indicate seismic lines. AND—Antarctic Drilling Project; DSDP—Deep Sea Drilling Project; DVDP—Dry Valley Drilling Project; FHDP—Friis Hills Drilling Project; CRP—Cape Roberts Project.

stratigraphic units from the bottom to top: Friis I, Friis II (lower and upper), and the Cavendish drifts (Lewis and Ashworth, 2016). Friis I drift sits on granitic basement within a small paleovalley on the eastern bench (Fig. 2D) and includes upper and lower diamictite units interpreted as subglacial (lodgement/traction) till. The diamictite units are separated by interbedded fluvio-lacustrine mudstone, sandstone, conglomerate, and volcanic ash. Friis I drift is not observed in outcrop in the Central Valley (Lewis and Ashworth, 2016).

Friis II drift sediments are located within the eastern paleovalley and across the Central Valley (Fig. 2D). Friis II lower drift comprises locally derived till sheets that represent the advance and retreat of wet-based, temperate-style glaciers flowing to the southeast, which is at odds with the modern glacial system. During interglacials, small fluvial systems linked retreated ice margins to small lakes separated by interfluves characterized by soils and peats. Fossiliferous beds recovered from Friis II drift lower sediments include micro- and macrofossils, including diatoms, megaspores, algal cells, pollen, moss stems, seeds, and fragments of insects. Three-dimensional leaf impressions record a *Nothofagus* shrub tundra vegetation. The complete fossil assemblage reflects mean summer temperatures of ~6–7 °C (Lewis and Ashworth, 2016). Sediments within the Friis II upper drift are generally fossil poor, weathered, and have a higher abundance of granite clasts (Lewis and Ashworth, 2016).

Cavendish drift occurs along the southern margin of the Friis Hills, where it blankets the surface at the mouth of the Central Valley and extends downslope toward the margin of the modern Taylor Glacier (Lewis and Ashworth, 2016; Fig. 2D). The drift comprises granite-rich diamictite units of up to 6 m thick and well-sorted sandy and silt interbeds of up to 2.6 m thick. Climbing ripples and cross-beds are common in the sand-rich units and indicate that water currents flowed north-

ward during deposition (Lewis and Ashworth, 2016). Fossil biota were not recovered from any of these finer grained units. Cavendish drift cuts underlying Friis II drift sediments and forms a series of benches that run parallel to the slope along the mouth of the Central Valley and create a series of “steps” that are inferred to get younger with decreasing elevation (Lewis and Ashworth, 2016). These stepped units are ablation till units that formed at the margin of the paleo Taylor Valley during a phase of major downcutting that formed the valley at the southern margin of the Friis Hills, which today dissects the Kukri Hills (Lewis and Ashworth, 2016).

Lewis and Ashworth (2016) presented a glacial history for the Friis Hills region that includes an early alpine phase (Friis I drift), late alpine phase (Friis II [lower] drift), transitional phase (Friis II [upper] drift), ice-sheet phase with thick ice sheets (no sediments preserved in the Friis Hills), and a reduced ice-sheet phase (Cavendish drift). Direct age control for this history is based on a radiometric $^{40}\text{Ar}/^{39}\text{Ar}$ age of 19.76 (± 0.11) Ma from the interglacial unit in the Friis I drift (Lewis and Ashworth, 2016). No direct age control was available for the Friis II and Cavendish drifts, but an inferred correlation to other directly dated deposits in the McMurdo Dry Valleys was used to suggest that the Friis II sediments were >14.1 Ma and the Cavendish drift was late Miocene (Lewis and Ashworth, 2016). Subsequent analysis of cosmogenic nuclides from sediments in Friis II drift suggested the Friis Hills drifts are older than 14 Ma (Valletta et al., 2015).

The Friis Hills Drilling Project

Distribution of the Friis Hills drifts and their geomorphic expression suggested that a more extensive stratigraphic record lay buried in the Friis Hills Central Valley. This observation, and the need to acquire additional age control on this important Miocene site, were the primary motivation for the Friis Hills Drilling Project (FHDP). A seismic refraction survey conducted in the austral summer of 2014–2015 revealed a low-velocity sequence of up to 60 m thick in the central Friis basin overlying significantly higher velocity, seismically opaque material interpreted as basement. In the austral summer of 2016–2017, sediment cores were collected from three locations in the Friis Hills Central Valley (Figs. 2C–2D). Two holes were drilled and cored at Friis Hills Drilling Project Site 1 (FHDP-1A and 1B), three at Site 2 (FHDP-2A, 2B, and 2C), and one at Site 3 (FHDP-3A). A composite of the cores recovered at each site provides a relatively continuous stratigraphic record (79% recovery) through the Friis II drift. Friis I drift was not recovered at any of the drill sites.

Here, we present a detailed sedimentological and lithostratigraphic analysis of the succession recovered by drilling. We develop a stratigraphic framework for the Friis II drift based on an integrated cyclo-, tephro-, magneto-, and biostratigraphy that offers unprecedented age control on these terrestrial sediments and allows correlation to the astronomical time series (Laskar et al., 2011; Laskar et al., 2004). Stratigraphic data from the drill cores are combined with seismic data and regional topography and geomorphology to interpret stratigraphic packages. We present a paleoenvironmental interpretation using this new stratigraphic information and preliminary paleoecological data that builds on the previous history developed by Lewis and Ashworth (2016). Finally, we incorporate this new terrestrial stratigraphy with offshore records and present an environmental history for the western margin of the Ross Sea and the East Antarctic Ice Sheet, through the MMCT.

METHODS

Core was recovered using conventional down-hole coring equipment and a cold weather modified, helicopter-portable Webster Drilling HPP 150 drill rig and chilled compressed air as a drilling fluid. An NQ2 drill string and coring assembly produced 50 mm diameter core that was cut into meter-long sections and placed into plastic half rounds. A visual description was produced for each core section on site. Each section was wrapped in lay-flat tubing, stored in ice-core boxes, and transported by helicopter to a freezer lab at Scott Base, where they were X-rayed. All cores were shipped to an ice-core facility at GNS Science in Lower Hutt, New Zealand, where they were re-examined and re-described if required. X-Ray CT data were collected at a medical imaging facility before discrete samples were taken using a tile cutting saw for sedimentological, paleomagnetic, paleontological, and geochemical analysis. An integrated age model was constructed using paleomagnetic reversal stratigraphy, which was correlated to the Global Polarity Time Scale (Gradstein and Ogg, 2020; Raffi et al., 2020), guided by numeric ages for two interbedded silicic tephra, and (limited) biostratigraphic constraints. Detailed methods used to derive results discussed below are reported in the Supplemental Material¹.

¹Supplemental Material. Detailed methods, a complete sample list and associated palynology counts, tephra classification data, siliceous algae counts, prevalent plant genera, and paleomagnetism analyses. Please visit <https://doi.org/10.1130/GSAB.S.20415480> to access the supplemental material, and contact editing@geosociety.org with any questions.

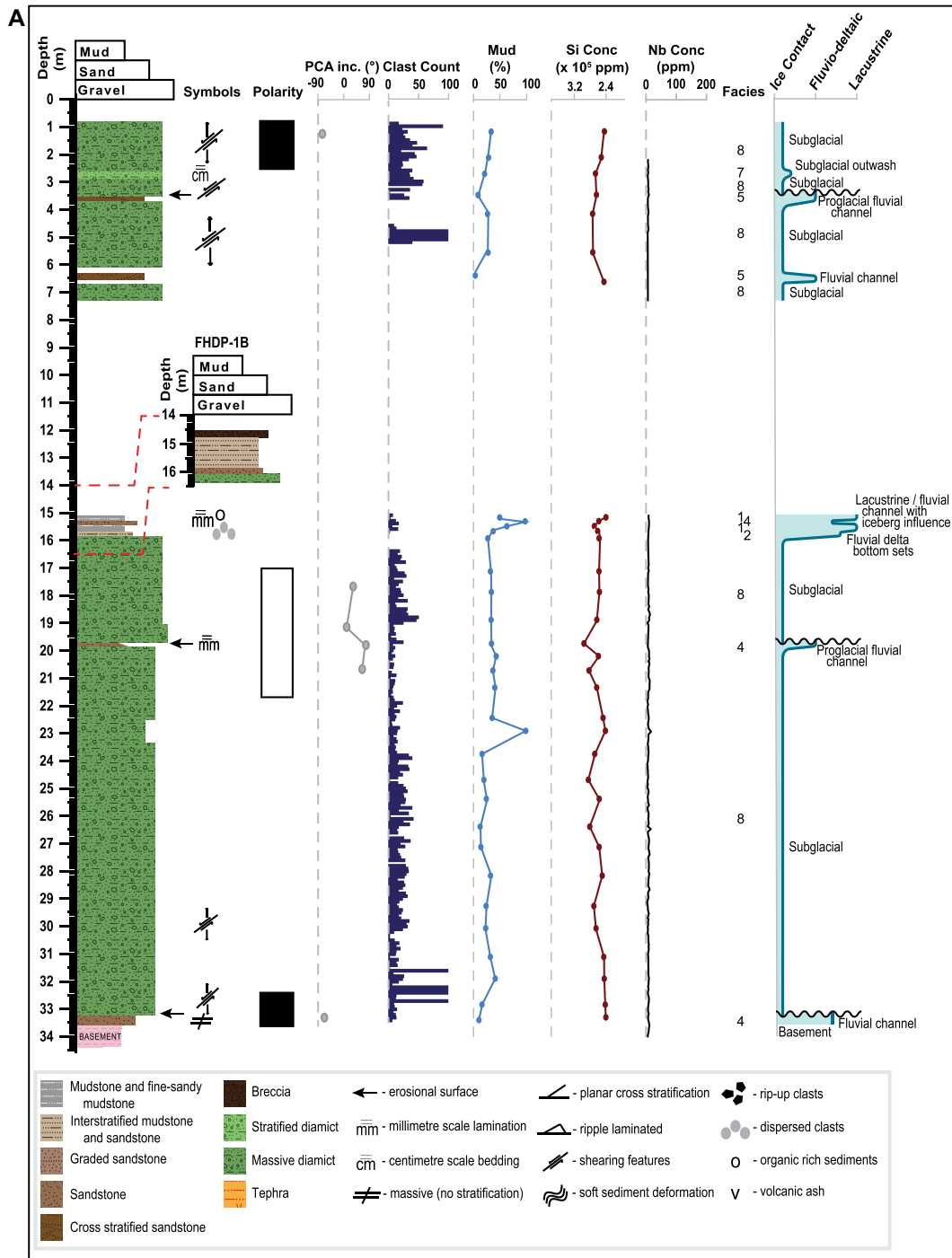


Figure 3. (A) Composite log of Friis Hills Drilling Project (FHDHP)-1A shows, from left to right, lithostratigraphy, paleomagnetic stratigraphy, sedimentology, geochemistry, and facies interpretation. Glacial surfaces of erosion (GSEs) define sequence/cycle boundaries on a glacial proximity curve. (B) Composite log of FHDHP-2A shows, from left to right, lithostratigraphy, paleomagnetic stratigraphy, sedimentology, geochemistry, and facies interpretation. Glacial surfaces of erosion (GSEs) define sequence/cycle boundaries on a glacial proximity curve. Note the depth and numeric age of tephra. (C) Composite log of FHDHP-3A shows, from left to right, lithostratigraphy, grain-size distributions, paleomagnetic stratigraphy, sedimentology, geochemistry, and facies interpretation. Glacial surfaces of erosion (GSEs) define sequence/cycle boundaries on glacial proximity curve. Note depth and numeric age of tephra. PCA—Principal Component Analysis.

RESULTS

Facies Analysis and Sequence Stratigraphy

A composite sequence through the Friis II drift reveals ~80 m of cyclic, fining-upwards facies successions comprising diamictite, sandstone, and mudstone facies, bounded by glacial erosional surfaces. Sixteen glacially influenced sedimentary cycles were identified in the three

FHDHP cores (Figs. 3A–3C). These cycles were defined as vertically stacked, repetitive facies successions identified by lithologic core descriptions, grain size analyses, and fossil content. Each sedimentary cycle is bounded at its base by a glacial surface of erosion (GSE) associated with the advance of a land-terminating alpine glacier system.

We identified nine recurring facies and summarize their characteristics and interpretation

along a depositional continuum from subglacial ice-proximal to proglacial grounding-line-distal lacustrine environments in Table 1 (See Appendix 1 for detailed facies descriptions and interpretations). The vertical occurrences of facies within cycles are shown for each drill site in Figures 3A–3C and in detail for cycle 5 in FHDHP-3A (Fig. 4). A 3-D conceptual depositional model for a cycle of glacial advance, early recession (proglacial lake terminating),

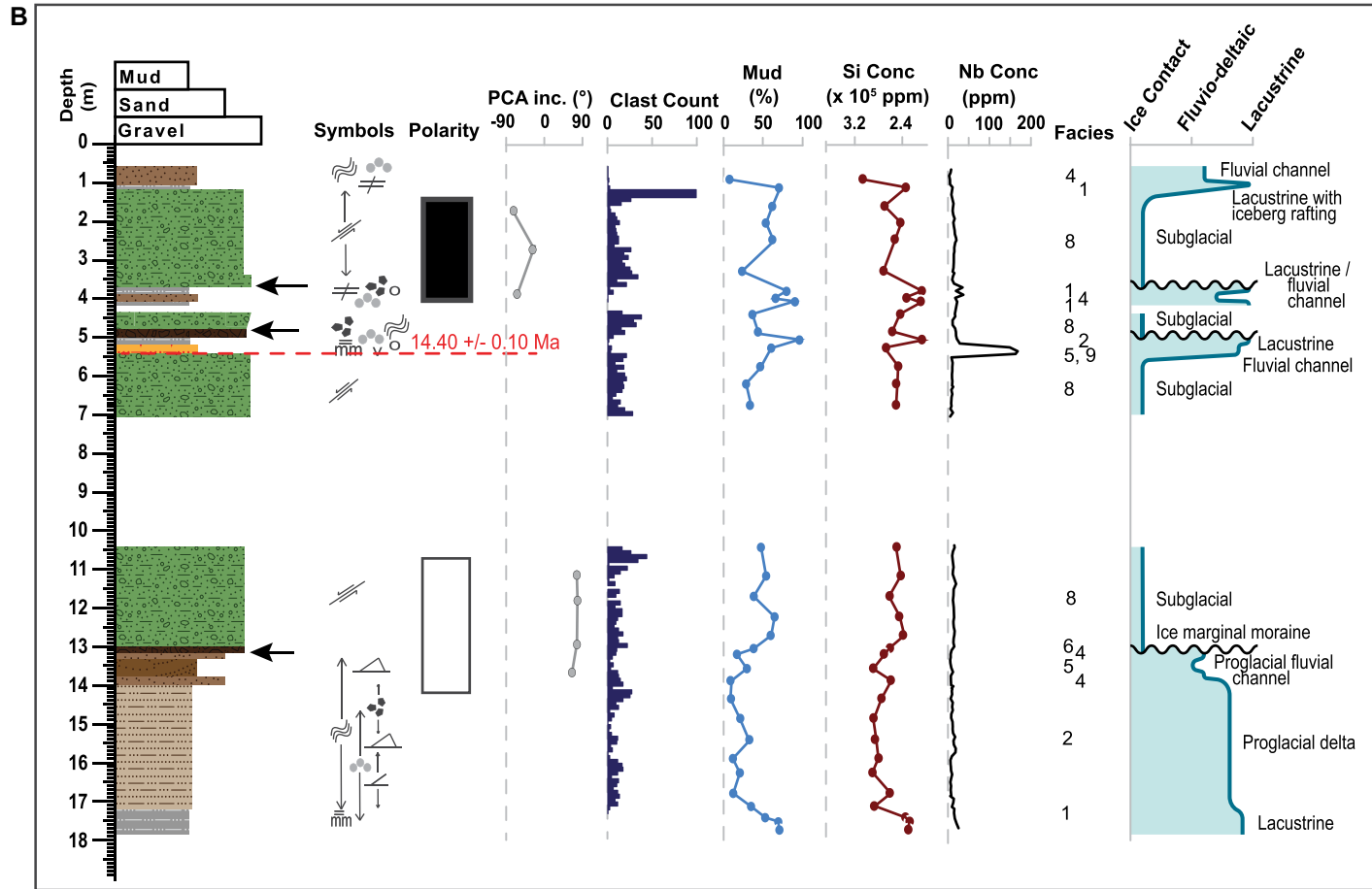


Figure 3. (Continued)

and late recession (proglacial land terminating) is shown in Figure 5.

Our model is based on the recognition of four repetitive facies successions preserved in successive cycles throughout the FHDP cores. Typically, cycles fine upwards from diamictites and breccia to sandstone and mudstone representing grounding-line retreat along the Friis Hills paleovalley. Subglacial environments at the drill sites transition to a proglacial, fluvio-lacustrine setting during warming intervals of deglaciation. Coarse-grained lithologies were deposited in subglacial and grounding zone proximal environments, whereas sandstones and mudstones represent fluvio-deltaic and lacustrine deposition under progressively lower energy depositional conditions. The tops of some cycles coarsen as grounding-line proximal and fluvio-deltaic sediments prograde over lacustrine facies during subsequent advance of the glacier forming the next GSE. Proglacial facies immediately underlying GSEs and subglacial facies above GSEs display a range of ductile and brittle deformation features, which are discussed below. Sedimen-

tary features observed in these facies are illustrated in Figures 6–8.

Subglacial Erosion and Deposition during Ice Advance

Sharp erosional surfaces that generally mark the base of each sequence are interpreted as GSEs, which have been observed and described from coastal glaciomarine settings where advancing ice grounds in marine environments (Dunbar et al., 2008; Fielding et al., 2011; McKay et al., 2009). Massive diamictite units (facies 8), typically between 0.5 m and 5 m thick, overlie deformed or brecciated glacio-fluvial or glacio-lacustrine lithofacies and generally reflect ice grounding and overriding in a subaqueous environment. The basal characteristics of these diamictites are consistent with known examples of subglacial deposition and overriding by grounded ice (Benn and Evans, 2010; Evans et al., 2006; Hart, 1996; Hart and Boulton, 1991; Hiemstra and van der Meer, 1997). The contact between the underlying interglacial units and overlying diamictite is often sharp, highly sheared, or contains

clastic intrusions (e.g., Figs. 6D, 6I, and 6J). Above the contact, the diamictite is physically intermixed with the underlying facies before grading upward into a massive diamictite that forms due to homogenization by subglacial shearing. Subglacial shear and ice loading are also indicated by syndepositional soft sediment deformation structures, intraclasts, and clastic dykes within diamictites, clast halos, and comet structures (e.g., Figs. 6B, 6E, and 6G) as well as compressional load features such as vertically cracked clasts (e.g., Figs. 6A, 6C, and 6F). Additionally, subglacial features are indicated by linear microstructures and a pervasive plasmic fabric (characterized by an oriented clay matrix) within diamictites and deformed sediments beneath diamictites.

Diamictites in FHDP-2 and FHDP-3 range in thickness, are dominated by locally derived clasts of Ferrar Dolerite and Beacon Sandstone, and generally contain a high percentage of mud and sedimentary features consistent with high levels of meltwater during glacial advance. In the stratigraphically younger FHDP-1A core, diamictite units are relatively thick (up to 12 m)

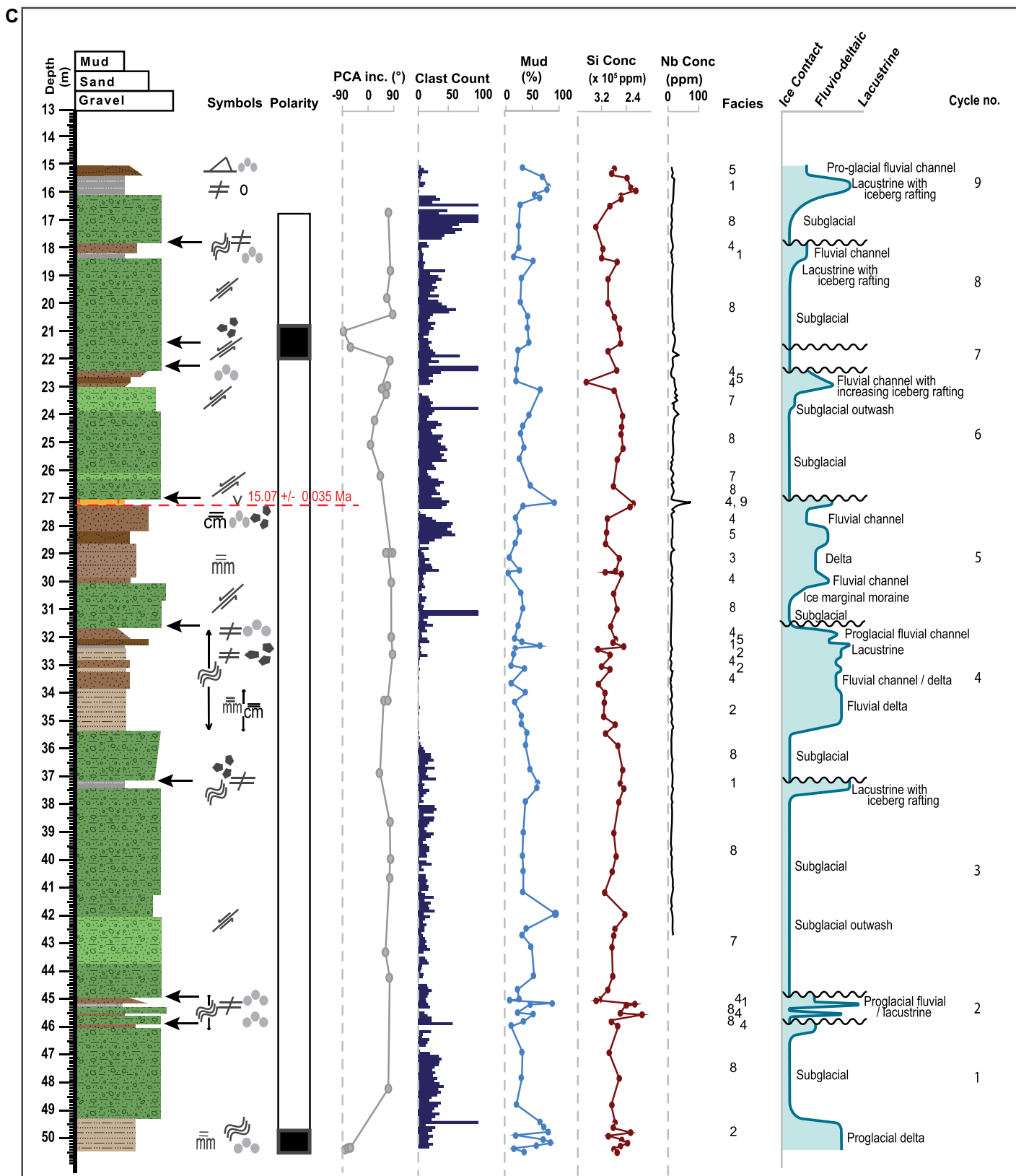


Figure 3. (Continued)

TABLE 1. SUMMARY OF LITHOFACIES CLASSIFICATION SCHEME

Facies	Name	Description	Interpretation	% of core	References
1	Mudstone and fine-sandy mudstone	Light-brown to dark-olive brown, organic-rich, massive to horizontally stratified, laminated and bedded, mudstone and fine-sandy mudstone with dispersed extraformational clasts of dolerite and granite.	Lacustrine bog under variable influence of iceberg or lake ice rafting	3.92	Fitzsimons (1992); Hiemstra and van der Meer (1997); van der Meer and Menzies (2011)
2	Interstratified mudstone and sandstone	Gray to brown, laminated and bedded (up to 5 cm thick), carbonaceous, horizontally interstratified, mudstone and fine sandstone with dispersed extraclasts of dolerite and granite.	Proglacial delta bottom set with iceberg or lake ice rafting (with dispersed clasts)	9.27	McCabe and Eyles (1988); Fitzsimons (1992); Walker and James (1992); Bennett et al. (2000)
3	Graded sandstone	Dark gray to olive and light gray, normally graded beds up to 30 cm thick, which contain poorly sorted, pebbly coarse sandstone that fines upwards into well-sorted, laminated fine sandstone.	Delta foreset, sediment gravity flows	1.94	Miall (1977); Eyles et al. (1987); Tye and Coleman (1989); Horton and Schmitt (1996); Bennett et al. (2000)
4	Sandstone	Gray to yellow brown, massive to horizontally bedded (up to 30 cm thick), moderately to poorly sorted, muddy-fine to pebbly coarse sandstone.	Fluvial channel/delta	6.91	Eyles et al. (1987); McCarroll and Harris (1992)
5	Cross-stratified sandstone	Yellow-brown to gray, well-sorted, cross-stratified fine to coarse sandstone.	Proglacial fluvial channel (with dispersed clasts)	2.85	Miall (1977); Porter and Beget (1981); Eyles and Eyles (1983); Thomas et al. (2004); Benn and Evans (2010)
6	Breccia	Light olive brown, clast-rich, poorly sorted breccia with a muddy sand matrix.	Sediment redeposition by mass flow, ice marginal moraine	0.45	Benn and Evans (1998); Atkins et al. (2002)
7	Stratified diamictite	Gray, clast-rich to clast-poor, sandy or muddy subhorizontal to high-angle weakly stratified (beds of up to 20 cm thick) diamictite.	Proximal subglacial outwash, sediment gravity flow, moraines, rain out of debris from ice	4.26	Hart (1990); Menzies (1989); McCarroll and Harris (1992)
8	Massive diamictite	Gray to yellow-brown, massive clast-rich to clast-poor, sandy to intermediate diamictite.	Deposition by flowing ice, subglacial	69.84	Van der Meer et al. (2003); Fitzsimons (1992)
9	Tephra	White/gray, deformed, massive to laminated, vitric, sandy mud to mud.	Volcaniclastic, remobilized in fluvial/lacustrine environment	0.56	

and lighter in color than in FHDP-2 and FHDP-3, which indicates a less weathered matrix. The thick diamictites in FHDP-1A commonly contain features that indicate compression and shearing. These features, along with an overall increase in clast numbers, including more abundant granitic clasts, indicate that glaciers that overrode the site were colder at their base and eroded and transported rocks from a more extensive region than stratigraphically older diamictites in FHDP-2A and FHDP-3A.

We interpret the GSEs and overlying massive diamictite facies as erosion surfaces and till sheets deposited by the southeastward advance and grounding of regionally and locally sourced alpine glaciers during cold climate glacial phases. Grounding often occurs across small proglacial lakes, where limited water depth does not significantly reduce ice load through flotation (Eyles et al., 1982). Within some massive diamictites that overlie GSEs, sharp local change in color and/or clast content could signify a change in glacial load, for example, a minor retreat followed by glacial advance within a lodgement till unit (Eyles et al., 1982; Miller, 1989).

Proglacial Deposition during Ice Retreat

Accurately identifying proglacial depositional environments based on some of the diamictite units in the FHDP cores can be difficult. Massive, homogeneous diamictites can form in sub-aerial and subaqueous proglacial environments such as fans and deltas as debris flows deposited

under the influence of gravity. Diamictites that lack deformation features associated with sliding and overriding ice and do not occur immediately above a GSE may represent pro-glacial deposition during grounding-line retreat or advance. Stratified diamictites that occur in association with massive diamictites may be deposited near the glacier margin in terminal and/or lateral moraines and as cohesive debris flows and rain-out deposits as the glacier terminus recedes (e.g., Fig. 5B) (McKay et al., 2009).

However, most subglacial tills in the FHDP cores are overlain by broadly fining-upwards facies successions ranging from 0.5 m to 4 m thick that include stratified diamictites (e.g., Fig. 7J); poorly sorted pebbly sandstones (e.g., Fig. 7G); well-sorted, cross-stratified sandstones (e.g., Figs. 7H–7I); normally graded sandstone beds (e.g., Fig. 7F); and interstratified mudstone and sandstone (e.g., Figs. 7C–7E). This recessional succession represents retreat of the glacier terminus up-valley toward the northwest onto surrounding highlands and the development of a small, fluvial-lacustrine delta system in the Central Friis Hills basin (Fig. 5C). Sediment transport and deposition occurred via tractional currents in river channels and subaerial and subaqueous debris flows. As meltwater supply increased, the lake systems broadened and deepened, and the sedimentary succession became increasingly more ice- and shoreline-distal and was characterized by hemipelagic mudstones and sandy mudstones, with a decreasing influence of iceberg rafted debris.

Interglacial Lacustrine Deposition

Organic-rich, 0.5–4.5-m-thick mudstones and laminated, fine, sandy mudstone units with rare iceberg-rafterd debris (e.g., Figs. 7A–7B) represent lacustrine deposition in an ice-distal environment during interglacial warm phases (Fig. 5C). These intervals occur throughout all of the FHDP cores. In many cases, these deposits contain *Nothofagus* macrofossils including cuticles, wood, and root fragments, which indicate that the region was occupied by swampy alpine shrub tundra, consistent with previous studies (Lewis and Ashworth, 2016). Fossilized freshwater diatoms generally indicate the lakes were low-energy and relatively shallow. The presence of feather barbs in several samples suggests that bird species occupied the Friis Hills during interglacial periods. Peat forms when the organic content in mudstones is high; these organic-rich lithologies correspond to fossil-bearing siltstone beds described in pit sections by Lewis and Ashworth (2016) in the Friis Hills II Lower Drift that contain *Nothofagus* leaf mats. The closest locality where modern representatives of the fossil taxa in the Friis Hills sediments occur today is near the tree line in southernmost South America, where mean summer temperatures are ~6–7 °C (Lewis and Ashworth, 2016). Based on the basic paleoecological information described herein, we suggest that each interglacial deposit represents broadly similar environmental and climatic conditions during which time the Friis Hills hinterland may have been ice-free or almost

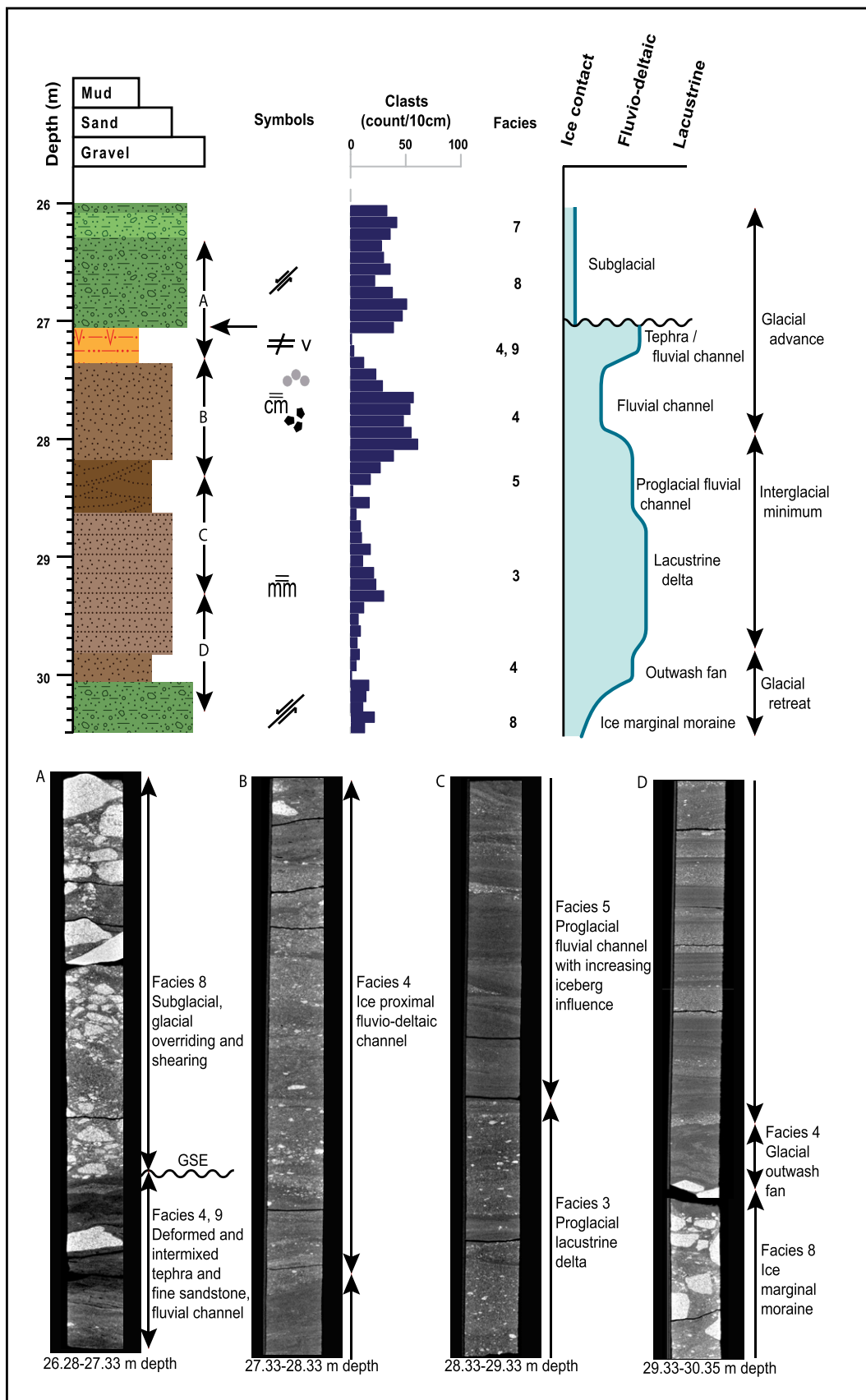


Figure 4. Example of a typical sedimentary cycle from Friis Hills Drilling Project (FHDPP)-3A (26.28–30.35 m; see Fig. 3C) shows (from bottom up) a retreat facies succession from grounding-line proximal diamictite to graded beds (Facies 4) deposited in an ice-distal lacustrine environment followed by a glacial advance succession, ice-overriding, and erosion. Geologic key is provided in Figure 3A.

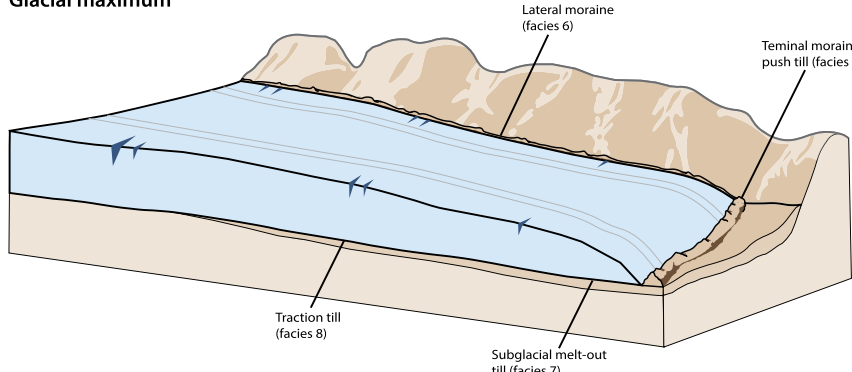
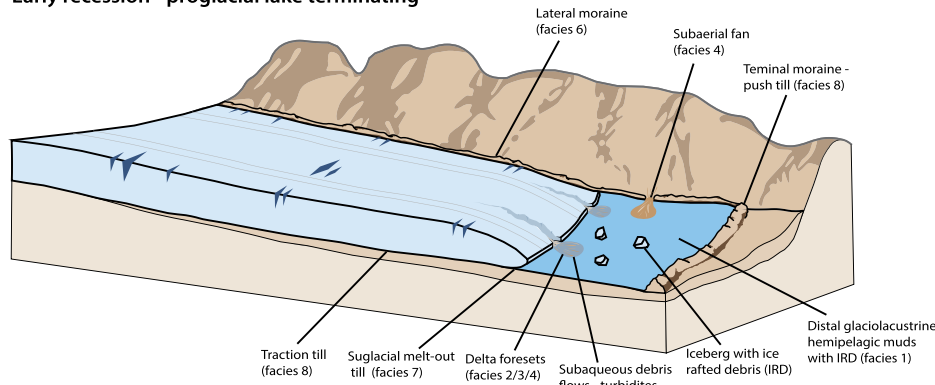
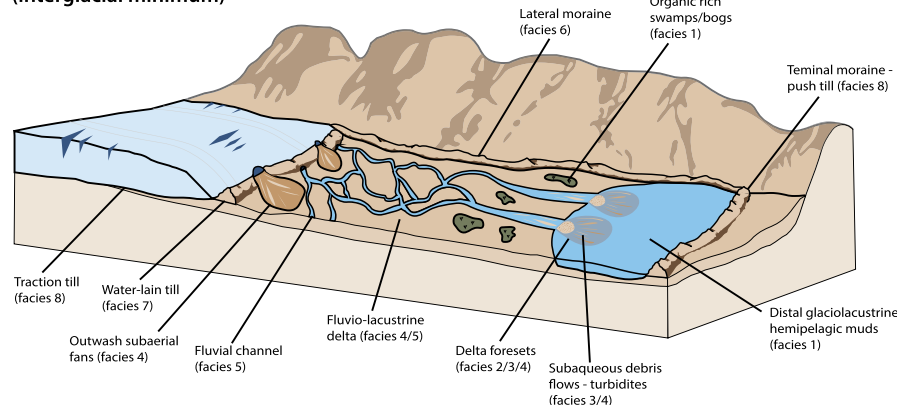
Glacial maximum**Early recession - proglacial lake terminating****Late recession - proglacial land terminating (interglacial minimum)**

Figure 5. Three-dimensional sedimentary depositional model for the Friis Hills central basin during the Middle Miocene Climate Transition shows facies and depositional environments associated with glacial maximum, early recession, and interglacial minimum phases of a glacial–interglacial climate cycle.

ice-free, consistent with previous studies (Lewis and Ashworth, 2016).

Proglacial Deposition during Ice Advance

In some sedimentary cycles, the interglacial lacustrine facies are overlain by a 0.5–5-m-thick, coarsening-upwards proglacial facies succession. This succession was first uncovered in Friis Hills soil pits (see Fig. 8; Lewis and Ash-

worth, 2016) and typically includes basal, subaqueous sediment gravity-flow deposits, such as interstratified sandstone laminae and beds and sequences of 5–50-cm-thick, graded sandstone beds that formed as a delta prograded toward and across organic-rich lake beds. These deposits commonly transition upwards into well-sorted, ripple cross-stratified sandstones deposited in river/stream channels. These fluvial deposits are

overlain by glacier terminus-proximal debris flow deposits comprising massive pebbly sandstones and stratified diamictites. The coarsening-upwards succession represents an increasing supply of sediment as the land-terminating ice front advanced down valley toward the lake. Associated deformation occurred as the glacier eventually overrode the fluvial-lacustrine environment. An increase in outsized clasts and dropstones upsection in lacustrine and delta-front facies indicates that icebergs were calving as the glacier entered the lake. Due to subglacial erosion at the glacial maximum, the full progradational facies succession is not always preserved in cycles below the GSE.

Paleobiology**Pollen and Spores**

Eighteen samples from interglacial sedimentary intervals (facies 1, 2, 4, and 5) in FHDP-1, FHDP-2, and FHDP-3 were examined for palynology. Pollen and spore abundance in the 18 samples was generally low and ranged from 0 to 146 specimens. Nine samples contained more than 30 pollen grains, with an average concentration of 4623 specimens/gram of sediment (see Supplemental Material). These samples were all taken from either sedimentary facies 1 (mudstone and fine, sandy mudstone) or facies 2 (interstratified mudstone and sandstone). Four samples containing fewer than 30 specimens/gram of sediment were collected from a mix of fine- and coarse-grained sedimentary facies (facies 1, 2, 4, and 5). Four barren samples were from facies 4 (sandstone) and 5 (cross-stratified sandstone). Palynomorph abundance varies with lithology; the highest numbers are preserved in the most ice-distal facies (see Supplemental Material).

Common elements in the Friis Hills samples include *Nothofagidites fusca* type, *Podocarpidites* spp., *Retitriletes* spp., and *Coptospora* spp. This assemblage is like that observed in early Miocene sediments in the Cape Roberts Project (CRP)-2A (Askin and Raine, 2000; Prebble et al., 2006) and Deep Sea Drilling Project Site 270 (Kulhanek et al., 2019) drill cores and poorly dated sediments from the Meyer Desert Formation of Oliver Bluffs in the central Transantarctic Mountains (Ashworth and Cantrill, 2004) and likely reflects tundra mosaic vegetation with low-growing *Nothofagus* and *Podocarpaceae* scrub occupying warmer sites. This palynomorph assemblage is common to most interglacial intervals through the entire Friis Hills sequence, and while there is some variability between interglacial intervals, there is no clear stratigraphic (temporal) pattern or trend. For example, samples at 37.16 m (L31229) and

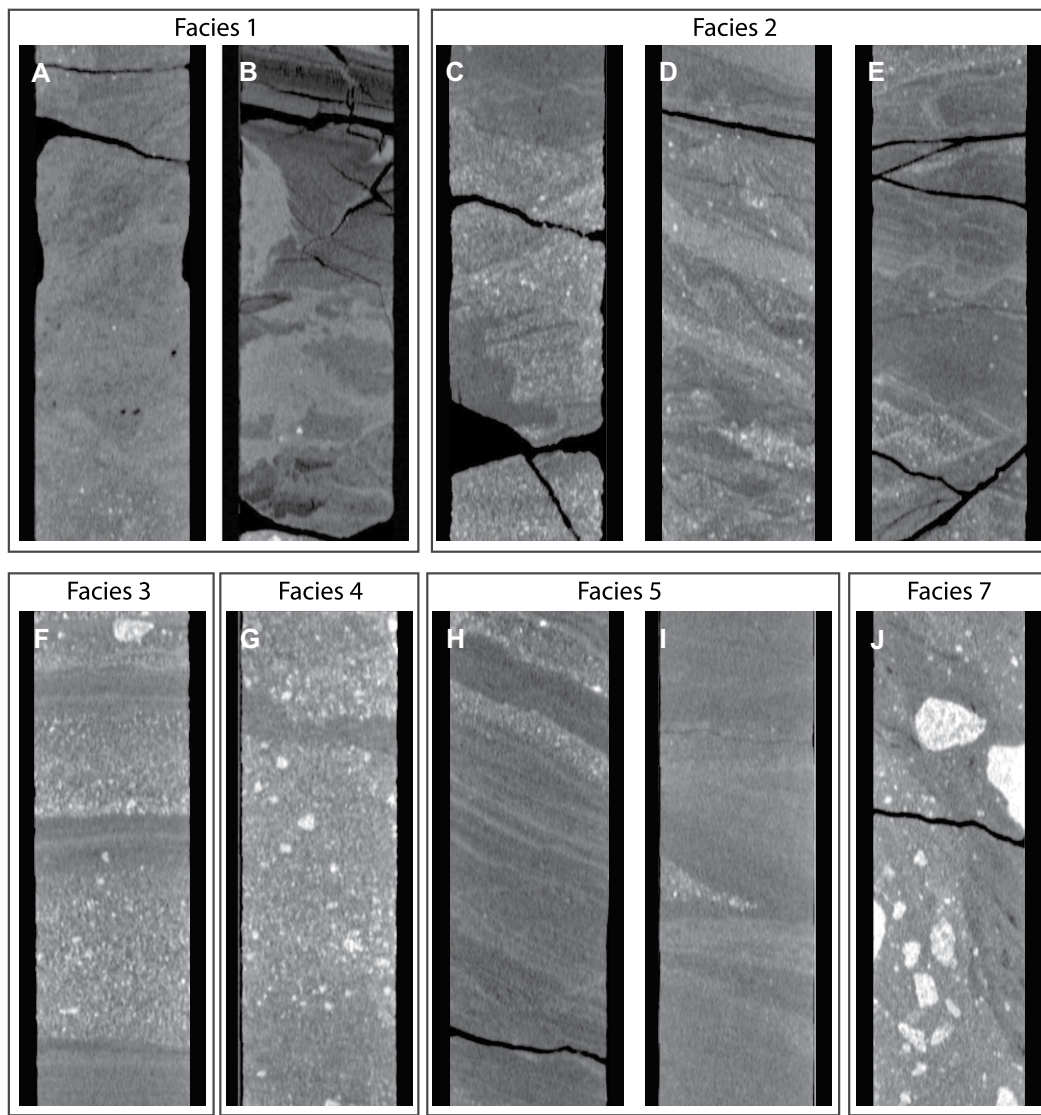


Figure 6. Sedimentary features observed in facies 1–7 are shown (also see Table 1). Mudstone and fine-sandy mudstone (facies 1): (A) Friis Hills Drilling Project (FHDP)-3A, 32.17–32.32 m, ductile deformation below glacial surface of erosion (GSE); (B) FHDP-3A, 37.17–37.31 m, highly sheared and deformed, with physical intermixing of lithologies, sediment injection, and brittle deformation below GSE. Interstratified mudstone and sandstone (facies 2): (C) FHDP-2A, 13.65–13.80 m, sedimentary intrusion; (D) FHDP-2A, 15.0–15.95 m, shearing and syn-depositional folding and slumping; (E) FHDP-2A, 16.19–16.35 m, high-angle reverse faults. Graded sandstone (facies 3): (F) FHDP-3A, 29.42–29.57 m, graded beds with sharp-based, pebbly sandstone passing up into fine, laminated sandstones. Sandstone (facies 4): (G) FHDP-3A, 27.60–27.75 m, weak decimeter-scale stratification defined by sharp-based pebbly sandstone. Cross stratified sandstone (facies 5): (H) FHDP-3A 22.67–22.82 m, high-angle cross stratification; (I) FHDP-3A, 28.62–28.77 m, high-angle planar cross bedding. Stratified diamictite (facies 7): (J) FHDP-3A 43.52–43.67 m,

deformed high-angle with clast and matrix alignment. Images are slices through X-ray computed tomography scans.

15.73 m (L31223) in FHDP-3A and at 15.73 m (L31223) in FHDP-1A all contain high pollen concentrations and assemblages with similar composition, including relatively abundant *Nothofagidites* and *Podocarpidites*. These data suggest that the range of environmental conditions that characterized interglacial episodes in the Friis Hills did not change through the time interval recorded in the Friis Hills sedimentary sequence.

Abundant Permian pollen is present in Beacon Sandstone (Askin, 1995) but is not found in the Friis Hills sediments. The absence of reworked Permian pollen, along with rare clusters of *Nothofagidites* pollen, imply a restricted catchment area and limited transport distance or limited erosion across the Friis Hills catchment. No marine palynomorphs were observed.

Diatoms

A total of 41 formally recognized diatom genera were observed across all samples examined in this study (Figs. S1–S3; see footnote 1). Most mudstone samples (facies 1–2) contained diatom remains, with the exception being the lower mudstones in FHDP-1A (>19 m down-hole) and FHDP-3A (seven samples deeper than 45 m). Diatoms were also present in some of the sandstones (facies 3–4) that were adjacent to or interstratified with mudstones.

The diatom flora is like that from the middle Miocene lake deposits of Mt. Boreas (Lewis et al., 2008) and includes shallow water plankton (e.g., *Staurosirella*, *Staurosira*, and chrysophycean flagellates) as well as benthic species that lived on mud, stones, mosses, and waterweeds (Figs. S1–S3). Overall, the diatom assemblages

at Friis Hills and Mt. Boreas bear little resemblance to modern Antarctic flora (Pinseel et al., 2021) and are more like assemblages that characterize low ionic-strength lakes and streams in the Arctic (Pinseel et al., 2021). These observations support the antiquity of the Friis Hills samples (see biostratigraphy) and suggest that the climate was more like that of modern Arctic tundra settings (e.g., Spitsbergen and Greenland) than that of Antarctica today.

Age Model and Chronostratigraphic Correlation

Biostratigraphy

Biostratigraphic constraints are limited as terrestrial biostratigraphic datums in Antarctica suffer from endemism, poor age

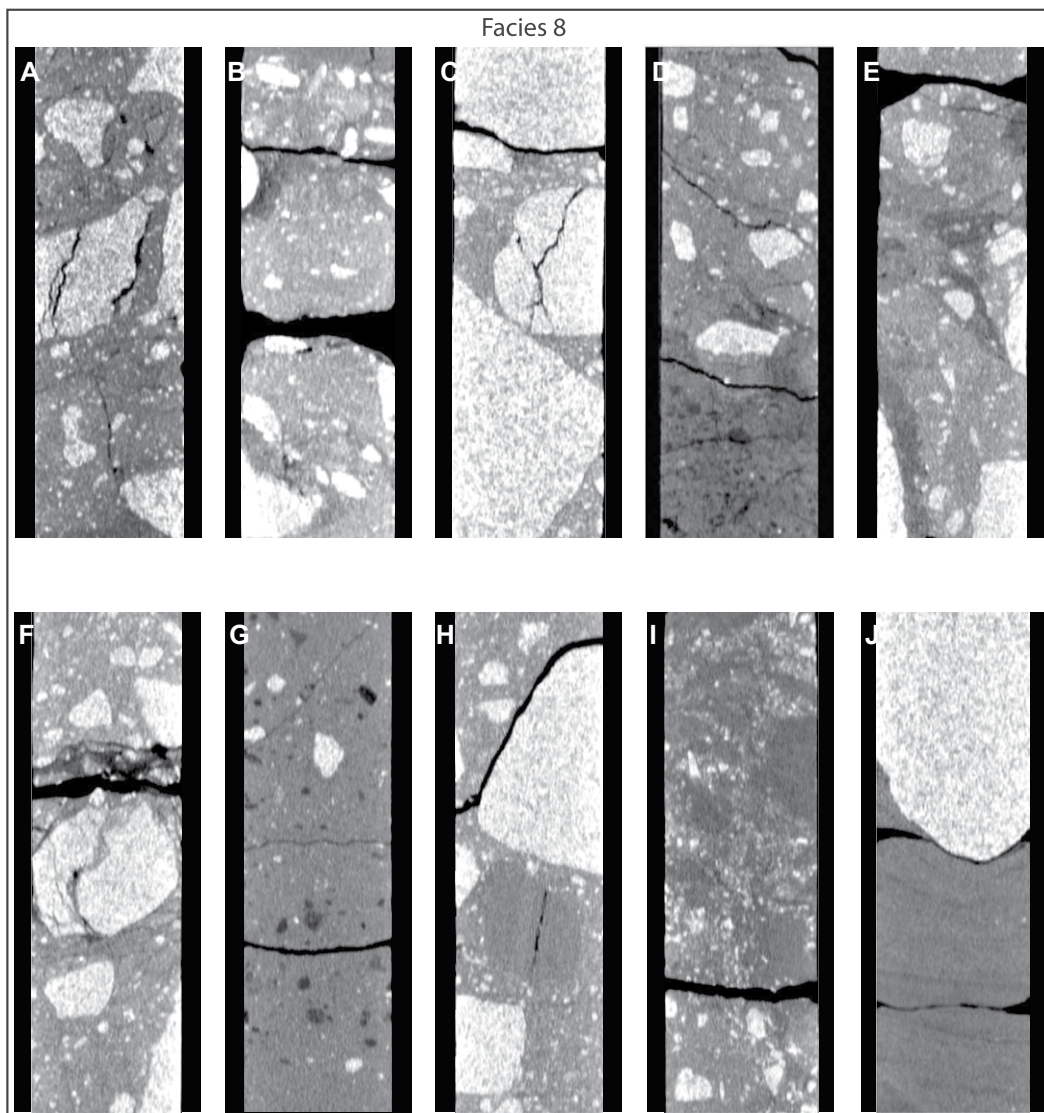


Figure 7. Sedimentary features observed in massive diamicrite (facies 8) are shown: (A) Friis Hills Drilling Project (FHDP)-1A, 2.42–2.57 m, vertically cracked clast, deformed plasmic fabric; (B) FHDP-1A, 22.94–23.09 m, clast halos, turbate fabric; (C) FHDP-1A, 25.56–25.71 m, vertically cracked clast; (D) FHDP-2A, 3.57–3.72 m, extraformational clasts (black = mudstone) and sedimentary injection; (E) FHDP-3A, 22.23–22.38 m, clast halo and comet structure; (F) FHDP-3A, 21.60–21.75 m, vertically cracked clast; (G) FHDP-3A, 36.60–36.75 m, extraformational clasts; (H) FHDP-3A, 38.00–38.15 m, vertically cracked clast of Beacon Group quartzite with lamination-parallel ice lens infill; (I) FHDP-3A, 41.87–42.02 m, shear zone at glacial surface of erosion; (J) FHDP-3A, 49.22–49.37 m, sag depression and deformation from dropstone. Images are slices through X-ray computed tomography scans.

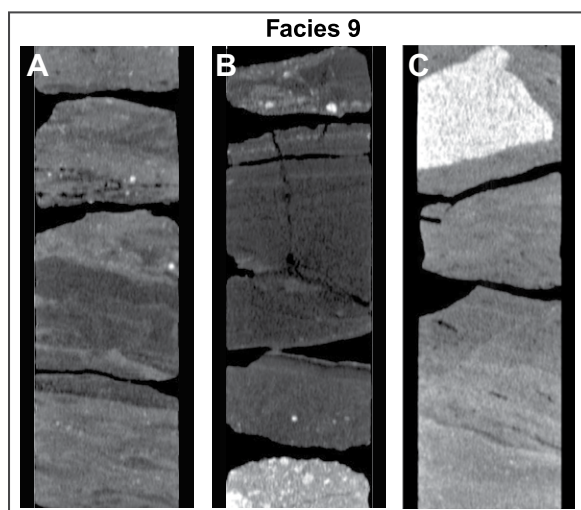


Figure 8. Tephra (facies 9) sedimentary features are shown. Tephra are redeposited in fluvial facies, are typically sharp-based, cross-laminated, and often fine-upwards. Vitric material is dark in color. (A) FHDP-2A, 5.12–5.27 m; (B) FHDP-2A, 5.27–5.32 m; (C) FHDP-3A, 27.10–27.25 m. Images are slices through X-ray computed tomography scans.

calibration, and a lack stratigraphic resolution compared to marine fossil datums generated from marine sedimentary sequences. Nevertheless, the pollen assemblage reported above for the interglacial facies is similar to that observed in early Miocene sediments in the CRP-2A drill core from McMurdo Sound (Askin and Raine, 2000; Prebble et al., 2006), the Antarctic Drilling Project (ANDRILL)-2A core (Warny et al., 2009), and Deep Sea Drilling Project (DSDP) 270 core from the central Ross Sea (Kulhanek et al., 2019; Fig. 2B). Although these flora are not generally age diagnostic, one observed taxon—*Tricolpites* sp. A—indicates that the sequence is younger than late Oligocene (Kulhanek et al., 2019). The Friis Hills assemblages also lack key elements of the more diverse Eocene assemblages

recovered from the Ross Sea McMurdo Erratics (Askin, 2000), which suggests very limited reworking during deposition of the Friis Hills sequences. Diatoms recovered from the Friis Hills sediments were not age diagnostic but are dissimilar to modern Antarctic assemblages.

Tephrostratigraphy and Tephrochronology

Tephra are preserved beneath GSEs in FHDP-2A/2C and FHDP-3A and are physically intermixed and deformed locally as pods and intraclasts of volcaniclastic sediment (e.g., Figs. 8A–8C). Major elemental composition of glass shards from the tephra in FHDP-2A/2C plot within the rhyolitic field (Fig. 9A). Shards from the tephra in FHDP-3A plot within the trachyte field (Fig. 9A). Glass chemistry from sample FHDP-2A/2C shows a bimodal population, with two shards exhibiting high SiO_2 (≥ 75 wt%) at comparatively low CaO (0.2 wt%) in comparison to the other shards, which cluster around 72 wt% SiO_2 at 0.4–0.6 wt% CaO (see Supplemental Material). The tephra in FHDP-3A has a SiO_2 concentration between 64 wt% and 68 wt% with comparatively high and diverse CaO values (0.6–1.6 wt%; Fig. 9). These major elemental data indicate that the two tephra layers derive from distinct eruption events and are not correlative.

Radiometric analysis of single crystals from each tephra layer (see Methods in Supplemental Material) indicates a numeric age of 15.07 ± 0.035 Ma for the tephra at 27.2 m in FHDP-3A and bimodal distribution of 15.59 ± 0.035 Ma and 14.4 ± 0.01 Ma for the tephra at 5.3 m in FHDP-2A (Fig. 10). These numeric data indicate maximum ages as the tephra are not primary and were likely reworked up section.

The age and major element oxide chemistry of the trachytic tephra in FHDP-3A preclude any direct correlation to known eruptive events. However, middle Miocene trachytic eruptions from Mount Morning are well-documented (Martin et al., 2010) and suggest that the volcanic center is the likely source of the FHDP-3A tephra. The bimodal rhyolitic glass from the FHDP-2A/2C core may also derive from Mount Morning, which has one known rhyolitic eruptive event dated at $15.4 \text{ Ma} \pm 0.1 \text{ Ma}$ in the Pinnacle Valley (Martin et al., 2010).

Paleomagnetism

Rock magnetic analyses indicate that magnetite is the dominant carrier of the characteristic remanent magnetization (ChRM), with minor contributions of higher-coercivity minerals in FHDP-2A (Fig. S5). Hysteresis data had median coercivity (H_c) values of 10.8 mT for core FHDP-3A, 19.2 mT for FHDP-2A,

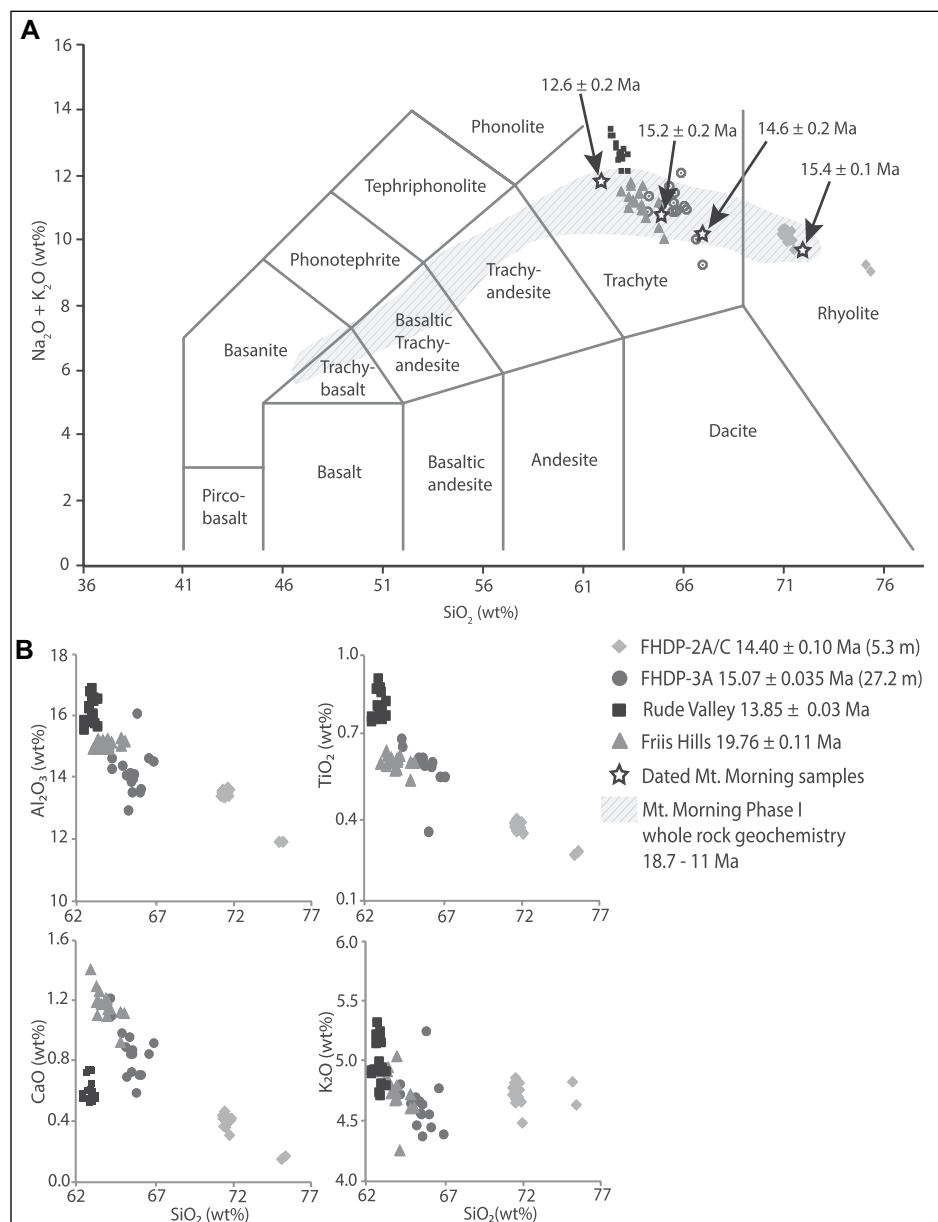


Figure 9. Major element glass chemistry data for the two new silicic tephra reported in this paper (Friis Hills Drilling Project [FHDP]-2A/C, 14.756 ± 0.035 Ma, and FHDP-3A, 15.075 ± 0.029 Ma), the 19.76 ± 0.11 Ma tephra from the Friis I unit reported in Lewis and Ashworth (2016), and a sample collected from Rude Valley dated at 13.85 ± 0.03 Ma (Lewis et al., 2007). (A) Total alkali versus silica (TAS) classification diagram (Le Maitre et al., 2002) shows that all tephra plot as trachyte except FHDP-2A/C tephra, which plots as a rhyolite of similar age and composition as the Mt. Morning Phase I eruption from Martin et al. (2010), which was dated by Kyle and Muney (1989) and Martin et al. (2010). (B) Major element bivariate plots differentiate FHDP-2A/C tephra from FHDP-3A tephra.

and 11.3 mT for FHDP-1A (Fig. S6A), and isothermal remanent magnetism (IRM) analyses (Fig. S6B) revealed low median coercivity of remanence (H_{cr}) values of 27.1 mT for FHDP-3A, 50.7 mT for FHDP-2A, and 30.7 mT for core FHDP-1A. First-order reversal curve (FORC) analyses of selected samples

from core FHDP-3A, where the number of samples and density is highest, indicate that low-coercivity minerals (such as magnetite) are dominant, with variable mixtures of single-domain and multi-domain grains (Fig. S6C) or of superparamagnetic and single-domain grains (Fig. S6D).

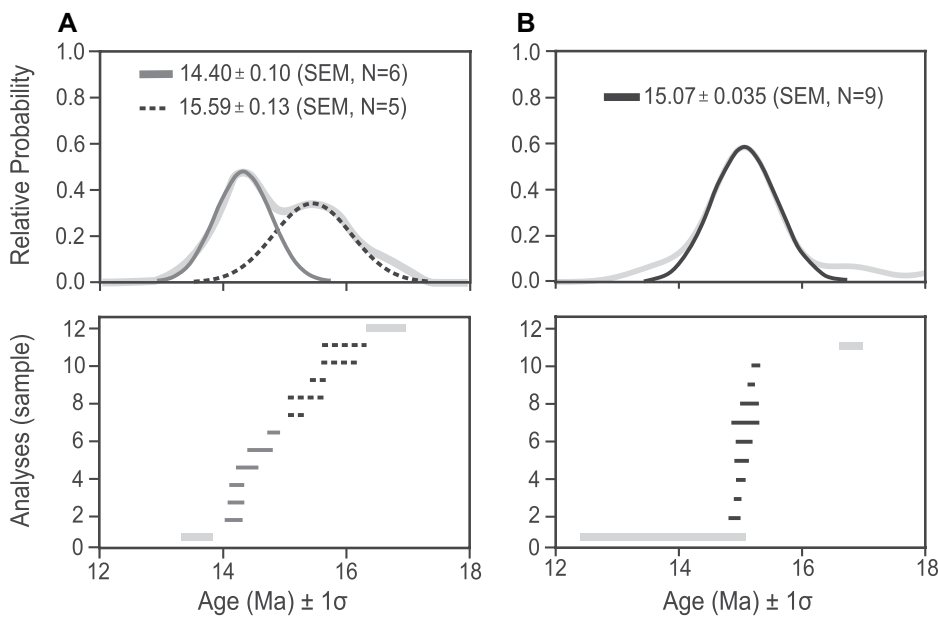


Figure 10. Age probability plots are shown for $^{40}\text{Ar}/^{39}\text{Ar}$ radioisotopic analyses of sanidine crystals from tephra in the Friis Hills Drilling Project (FHDP) cores. (A) FHDP-2A/C at 5.3 m depth, and (B) FHDP-3A at 27.2 m depth. SEM—Scanning Electron Microscope.

Representative demagnetization data were plotted on orthogonal component vector plots (Fig. S7) to inform the fitting of principal component analysis (PCA) directions for polarity determinations of the ChRM, which we assume is a detrital remanent magnetization (DRM). Glaciogenic sediments in all three cores contain large clasts of basement rocks, which can have strong magnetizations that overwhelm the DRM of the sediment matrix, resulting in spurious magnetizations. Although we tried to avoid large clasts during sampling, some samples still had spurious magnetizations. We have too few samples to allow division of the data into statistically significant categories; however, three broad groups of demagnetization behavior are apparent. The first group of samples (Figs. S7A–7D) had easily interpreted normal or reversed polarity magnetizations with a steeply inclined, linear component between 20 mT and 100 mT that was directed toward the origin and which we interpret to be the ChRM. The signal-to-noise ratio is high, with PCA Maximum Angular Deviation (MAD) values typically between 1° and 5° . A low-coercivity normal polarity component was observed in most reversed polarity samples, which varied in strength from very strong to weak. Such steeply inclined vertical overprints are commonly observed in high-latitude drill core samples (Florindo et al., 2005; Wilson et al., 2012). We interpret this low-coercivity normal polarity component to be a viscous remanent magnetization (VRM) that resulted from rotary drilling of the sediment core.

The second group of samples displayed magnetizations that do not relate to the geomagnetic field at the time of deposition. Samples (Fig. S7E) often had linear demagnetization trajectories that were directed to the origin, but the inclination of magnetization was too shallow and demagnetization behavior abnormal (e.g., with higher coercivity than that of other samples). We interpret these samples to contain strongly magnetized clasts of basement rock that overwhelmed the magnetization of the surrounding matrix. The remaining samples could not be interpreted. They had noisy demagnetization data or did not display a single, clear component (data were either offset from the origin or centered about the origin).

Magnostratigraphy

The longest continuous magnostratigraphy is from FHDP-3A, which contains 33 samples with stable magnetization on which PCA was conducted. Six samples had magnetization inclinations that are too shallow and probably were caused by the presence of a strongly magnetized clast in the sample (marked in gray, Fig. S5). The remaining samples had demagnetization data that varied in quality from very good with a low noise level and MAD values below 10° (20 samples) to a higher noise level with a maximum MAD of 17° (22.24 m). A down core reversed-normal-reversed-normal (R-N-R-N) pattern of magnetozones is identified with the 3R1–3N1 transition between 20.7 m and 21.14 m, the 3N1–3R2 transition between 21.8 m and

22.14 m, and the 3R2–3N2 transition between 48.9 m and 50.7 m depth (Fig. S5).

FHDP-2A contains six samples that had stable magnetization, which we attribute to a geomagnetic field origin, and one sample that has a shallow magnetization that is likely controlled by a clast. Seven more samples had very noisy demagnetization data and were not interpretable. Two samples at 1.75 m and 3.92 m have stable magnetizations with relatively low MAD values (4.3° and 8.4° , respectively). The magnetization of these samples likely resulted from deposition in a normal polarity field, which we use to define magnetozone 2N1. Between 11.22 m and 13.68 m are four well-behaved, reversed polarity samples (magnetozone 2R1), which have MAD values of between 13° and 3.1° . Although these samples are highly discontinuous, due to poor core recovery and unsuitable lithologies for sampling, we have tentatively identified a down core N-R zonation stratigraphy for FHDP-2A.

FHDP-1A has only four samples with stable magnetization that we suggest are associated with the contemporary geomagnetic field. An isolated normal polarity sample at 1.83 m displays noisy demagnetization data, and a MAD of 11.8° defines magneto zone 1N1 (Fig. S5). Two samples at 20.48 m and 21.35 m have reversed polarity inclinations (magnetozone 1R1) of 71.8° and 62.26° and corresponding MAD values of 9.3° and 18.8° . An isolated sample at 33.98 m near the bottom of the drill core has a well-behaved normal polarity demagnetization path with a strong normal polarity overprint. Therefore, like FHDP-2A, based on the limited available data we interpret an N-R-N down-core magnetic zonation stratigraphy for FHDP-1A.

Integrated Chronostratigraphy

Our age model (Fig. 11) is primarily based on the correlation of magnetozones to the Global Polarity Time Scale (Gradstein and Ogg, 2020; Raffi et al., 2020) and is constrained by radioisotopic ages of the two tephra. We use stratigraphic relationships observed in the field, basin geomorphology, and seismic refraction profiles to guide stratigraphic correlation of drill sites and across the basin (Fig. 12). The tephra layer in FHDP-3A provides a maximum age of 15.07 ± 0.035 Ma for the stratigraphic horizon at 27.2 m. However, the tephra occurs within an interval of reversed polarity (magnetozone 3R2), which suggests that the dated sanidine crystals were reworked up section, consistent with sedimentological evidence of remobilization in a fluvial environment. Based on these stratigraphic relationships, we correlate the interval from 50.3 m to 21.9 m to C5Bn.1r (15.032–14.870 Ma). We estimate an average sedimentation rate of 16 cm k.y.^{-1} for this well-constrained interval (Fig. 11). We

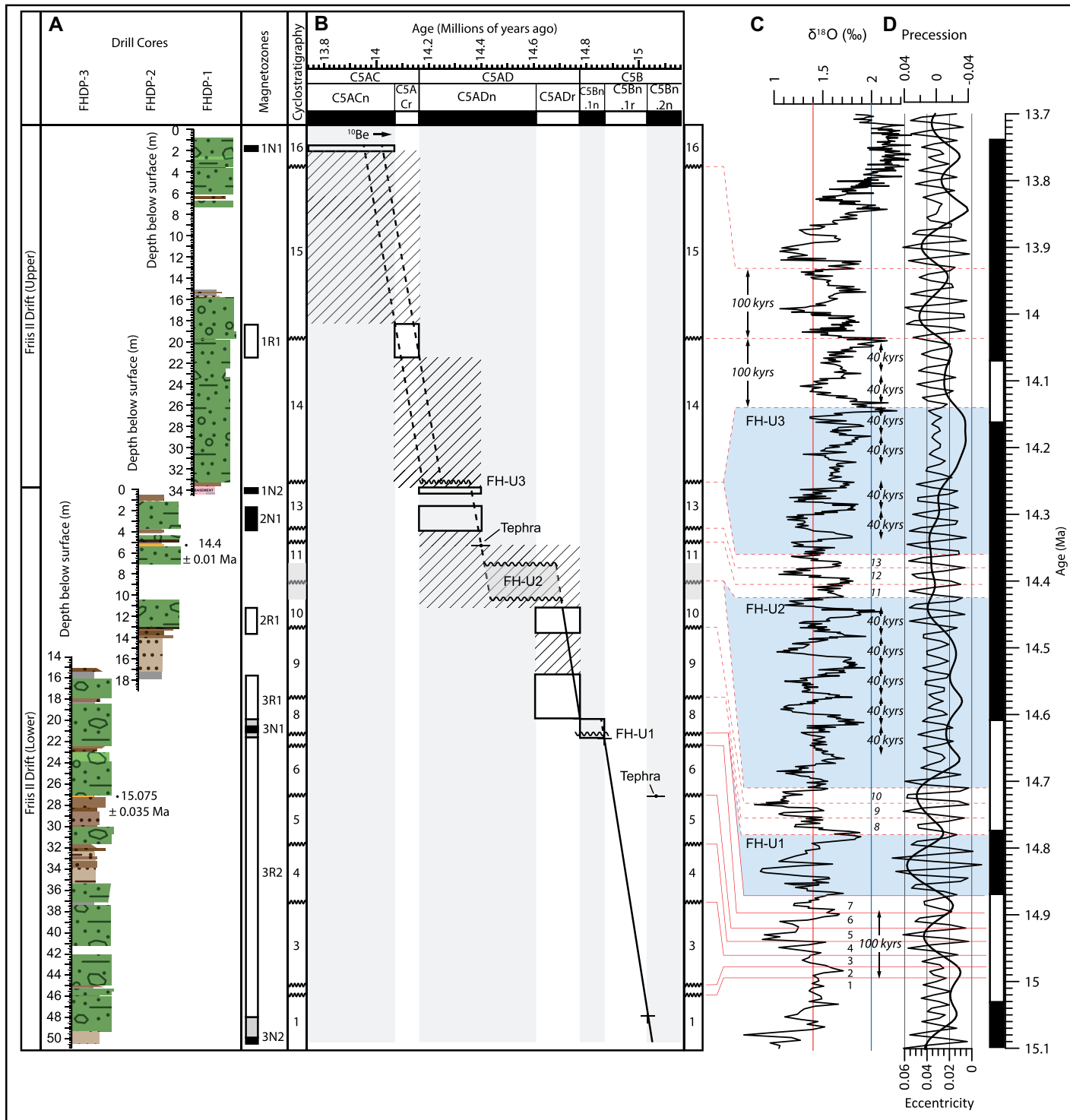


Figure 11. Age model for the Friis II drift recovered in drill cores from the Friis Hills central basin is shown. (A) Composite drill-core stratigraphy with magnetozones and cyclostratigraphy. (B) Line of correlation (LOC) between the composite and global polarity timescale. Boxes with solid lines indicate areas through which the LOC must pass. Hashed zones indicate regions of lower certainty. ^{10}Be date indicates approximate minimum age at surface (Valletta et al., 2015). (C) Deep-sea oxygen isotope compilation (De Vleeschouwer et al., 2017). (D) Astronomical precession and eccentricity cycles (Laskar et al., 2011). Proposed correlation between sedimentary cycles and astronomical cycles indicated by red lines (dashed lines = lower certainty). Blue zones indicate time missing in unconformities.

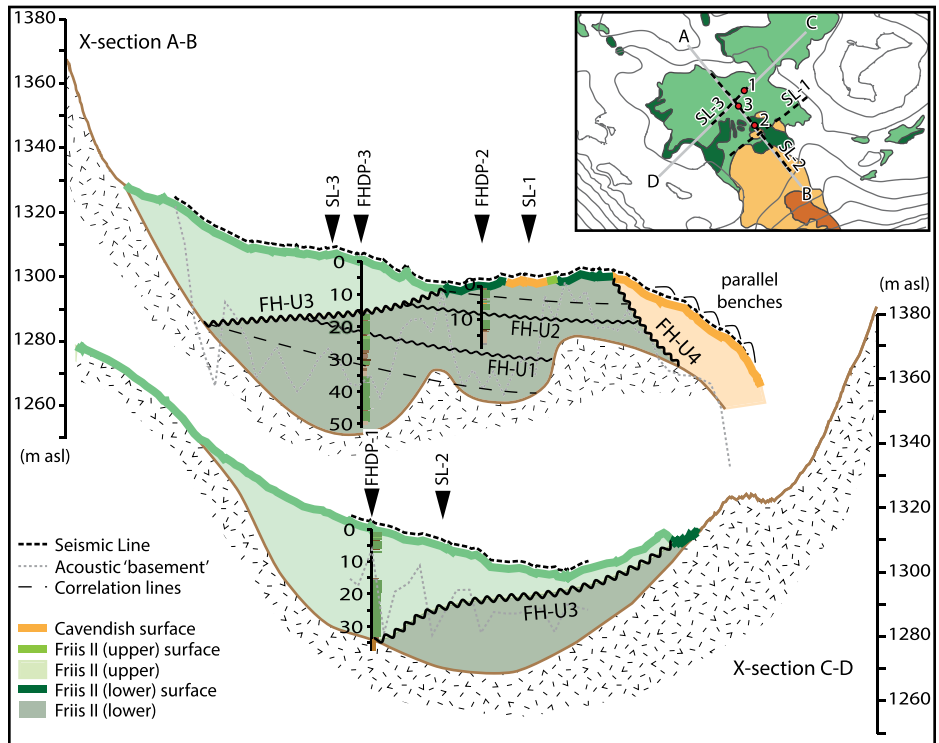


Figure 12. Geological cross-sections through the Friis Hills central basin are shown. Depth to crystalline basement is based on seismic refraction (gray dashed line) and drill-core data. Surface extent of Friis Hills II drift (upper and lower) and Cavendish drift is from Lewis and Ashworth (2016). Arrows indicate location of drill cores and crossing seismic lines. Inset: Location of cross-sections is indicated by gray lines. Dashed black lines indicate extent of seismic refraction survey lines 1, 2, and 3.

correlate the normal magnetozone 3N2 below 50.3 m to C5Bn.2n (15.160–15.032 Ma) and 3N1 between 21.9 m and 20.87 m to C5Bn.1n (14.870–14.775 Ma) and reversed magnetozone 3R1 above 20.87 m to the base of C5Adr (14.775–14.609 Ma). We infer that ~60–90 k.y. of time is missing within a disconformity in magnetozone 3N1 (FH-U1; Fig. 11).

The radioisotopic age of the tephra at 5.3 m in FHD-P-2A exhibits a bimodal distribution, which indicates that the tephra has a mixed age population and includes material from at least two eruptive events (Fig. 9B). We use the youngest age (14.4 ± 0.01 Ma) as a maximum constraint for our age model. This requires the age of normal magnetozone 2N1 (between 3.92 m and 1.75 m) to be younger than 14.4 Ma. Therefore, the interval from ~1–4 m most likely correlates to the upper part of C5Adn (<14.4 Ma to >14.163 Ma). Poor quality paleomagnetic data between 4 m and 7 m and poor core recovery from 7 m to 10 m preclude location of the magnetic reversal boundary that must occur in this interval. We correlate the stratigraphically lower magnetozone 2R1 (13.68–11.22 m) to C5Adr (14.775–14.609 Ma) and infer that the base of

FHD-P-2A correlates to ~15 m in FHD-P-3A (Fig. 11). A line of correlation (LOC) that originates at reversal 3N1/3R1 (C5Bn.1n/ C5Adr) and maintains the slope of the well-constrained lower section in FHD-P-3A passes through reversal 2R1 and supports our inferred correlation of FHD-P-3A and the lower section of FHD-P-2A. The age of the section between the top of 2R1 at 11.2 m and the tephra at 5.3 m in FHD-P-2A is difficult to precisely constrain. Our correlation/age model requires that this part of the sequence be condensed or missing in an unconformity (FH-U2), but we cannot identify which as core was not recovered. Sediments below this interval must be >14.6 Ma, and those above are 14.4 Ma or younger. If we assume the average sedimentation rate was relatively constant, we can apply a LOC to the poorly constrained interval with similar slope to the underlying sequence. If we assume this LOC must pass through the tephra, we can constrain the age of the upper 10 m of FHD-P-2A to between ca. 14.44 Ma and ca. 14.36 Ma (Fig. 11). This correlation implies that at least 240 k.y. of record is missing somewhere within the interval between 7 m and 10.5 m (FH-U2) in FHD-P-2A.

Chronostratigraphic constraints in FHD-P-1A and FHD-P-1B are limited. Magnetostratigraphic data from FHD-P-1A are limited to six reliable samples that suggest normal polarity at the base of the core, an interval of reversed polarity in the middle, and a normal interval at the top (Fig. 11). We cannot confidently correlate these magnetozones to the GPTS due to an absence of independent biostratigraphic or radioisotopic age control. However, sedimentological and glaciological characteristics of the diamictites in FHD-P-1A suggest they are most like diamictites in the Friis II drift (upper) of Lewis and Ashworth (2016). Diamictites in FHD-P-2A and -3A are like those in the Friis Hills II lower drift of Lewis and Ashworth (2016). Based on this evidence, we suggest that sediments at the base of FHD-P-1B sit stratigraphically above the top of FHD-P-2A and that magnetozone 1N2 correlates to C5Adn (14.609–14.163 Ma). Reversed magnetozone 1R1 is then correlated to C5ACr (14.163–14.070 Ma) and the normal magnetozone 1N1 at the top of FHD-P-1B to C5ACn (14.070–13.739 Ma). If we assume the sedimentation rate at FHD-P-1A was like that at FHD-P-3A, we can apply an LOC to FHD-P-1A with similar slope. This LOC must pass through reversed magnetozone 1R1 (Fig. 11). This interpretation suggests that the sedimentary sequence in FHD-P-1A is younger than ca. 14.25 Ma and older than 13.95 Ma, which is consistent with a minimum age assignment for the Friis Hills succession of 14 Ma based on meteoric ^{10}Be analysis (Valletta et al., 2015). However, the maximum age for the Friis Hills sequence presented herein (ca. 15.1 Ma) is younger than was suggested by Valletta et al. (2015) and indicates that sediments in the Central Valley were deposited at the termination of the MCO and through the MMCT. Furthermore, the age model indicates that the Friis Hills succession is discontinuous, with significant disconformities at the base of FHD-P-1A and within FHD-P-2A, which imply that episodes of erosion (depositional hiatuses) occurred across the Central Valley between 14.7 Ma and 14.2 Ma.

Composite Stratigraphy of MMCT in Central Valley, Friis Hills

We integrate topographic profiles, previous mapping (Lewis and Ashworth, 2016), new drill core stratigraphy, and seismic refraction survey data to derive a basin geometry and stratigraphic architecture of the basin fill for the central Friis Hills (Fig. 12). Below, we present an updated environmental history for the Friis Hills by integrating our new drill core stratigraphy within the stratigraphic framework established by Lewis and Ashworth (2016). Importantly, new

chronostratigraphic constraints from the more continuous and complete FHDp drill cores allow us to further refine and expand upon the observations and reconstructions provided by Lewis and Ashworth (2016).

Friis II Drift (Lower)

We correlate Friis II drift (lower) with a ~53-m-thick composite interval recovered in FHDp-3A and FHDp-2A that was deposited between 15.1 Ma and 14.4 Ma and comprises 13 vertically stacked, glacial–interglacial sedimentary cycles. This sequence includes eight-and-a-half cycles in FHDp-3A and four-and-a-half cycles in the stratigraphically superjacent FHDp-2A drill core (Fig. 11). Drilling in the middle region of the Central Valley allowed us to recover a thicker, more complete interval of cyclic sedimentation that is equivalent to four cycles originally identified by Lewis and Ashworth (2016). Whereas the thickness and stratigraphic architecture of the cycles in the FHDp cores are remarkably like those described from shallow pits and outcrop, there were notable differences. For example, we did not observe iron-stained, weathered surfaces and boulder pavements at the top of till units and below lacustrine and/or fluvial facies that were deposited during glacial retreat. Instead, we record a gradational recessional facies succession that grades from coarse-grained, ice-proximal facies into finer-grained, fluvial-lacustrine facies. In some cases, the transition is abrupt, but we did not find evidence for incipient soils or weathered surfaces at the top of diamictites. These subaerial exposure features may have only formed at the margins of the Central Valley, where Lewis and Ashworth (2016) described many of their sections.

While we recovered moss, pollen, diatoms, insect remains, wood, and some leaf and root fragments in interglacial intervals, we did not find intact *Nothofagus* leaf impressions in the drill cores. However, we can correlate the fossiliferous interglacial fluvial-lacustrine facies between 4 m and 5 m depth in FHDp-2A with leaf beds that are exposed at the same elevation but within in a topographic low 400 m to the west of the drill site (Fig. 2D). These fossiliferous beds occur above the tephra layer in the core and indicate that the leaf fossil beds are younger than 14.4 Ma.

Friis II Drift (Upper)

FHDp-1A drilled directly into Friis II drift (upper) sediments, sampled ~33 m of the sequence, and terminated in dolerite basement. We infer that this sequence filled a channel that cut through Friis II drift (lower) sediments, creating a basin-wide disconformity ~200 k.y. in duration (Figs. 11–12). Complete recovery

of the Friis II drift (upper) at the FHDp-1A site was not achieved due to core loss through sections that were not ice cemented. However, three diamictite-dominated cycles, comprising sharp-based, heavily deformed massive till units of up to 13 m thick (Fig. 3A) overlain by thin, 0.5-m-thick intervals of organic-rich, lacustrine/peat bog lithologies and fluvial facies, were preserved. Fossiliferous deposits were not reported in the Friis II drift (upper) sediments by Lewis and Ashworth (2016). Diamictites in the core lack evidence for significant subglacial water during deposition and exhibit brittle and ductile deformation features associated with glacial loading and shearing. These sedimentological changes are consistent with a transition to a colder climate and thicker, more extensive dry- and cold-based ice cover across the Friis Hills during glacial episodes between ca. 14.4 Ma and 13.9 Ma. However, we note that interglacial facies were similar in sedimentological character and fossil content to those recorded in the Friis II drift (lower) unit. FHDp-3A also drilled directly into Friis II drift (upper) sediments, but core was not recovered as the sequence was dry and disintegrated during drilling.

Cavendish Drift

The drift cuts Friis Hills II drift (lower) sediments at the mouth of the Friis Central Valley. We did not penetrate sediments of the Cavendish drift during drilling, so the sequence clearly post-dates Friis Hills II drift as previously noted by Lewis and Ashworth (2016).

DISCUSSION

Antarctic Ice Sheet Evolution and Variability during the MMCT

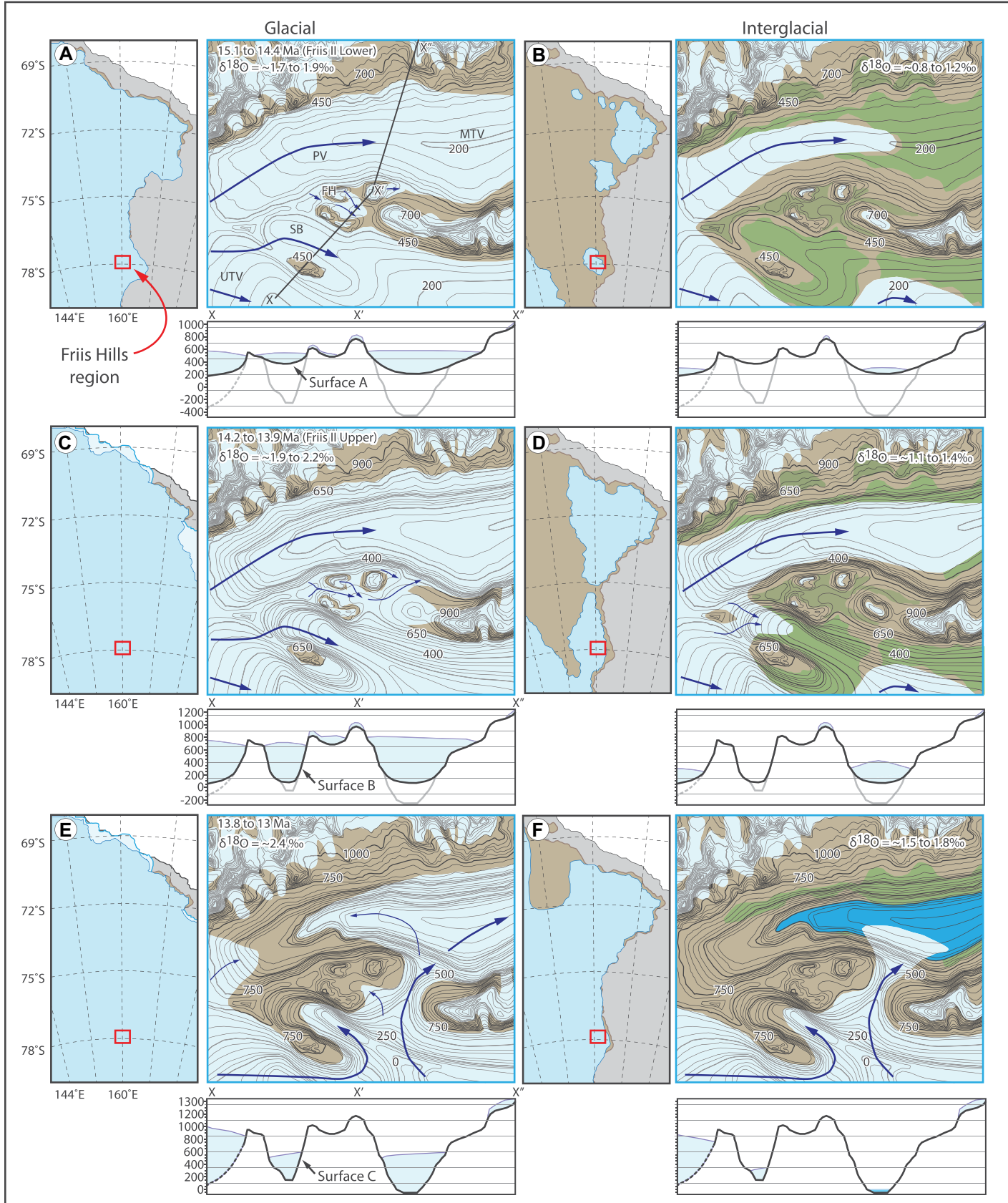
The new FHDp drill cores span the interval from 15.1 Ma to 13.9 Ma and offer an unprecedented opportunity to reconstruct the glacial history of the region from the termination of the MCO and through the MMCT (Fig. 13). Here, we integrate FHDp data with data from previous geological and geomorphological studies (Lewis and Ashworth, 2016; Lewis et al., 2006; Sugden et al., 1995), the ANDRILL-2A drill core (Levy et al., 2016), IODP Site 1531 (Marschalek et al., 2021; McKay et al., 2019), and seismic records from McMurdo Sound (Brancolini et al., 1995) and the Ross Sea (Colleoni et al., 2018; De Santis et al., 1995; Pérez et al., 2021). We provide new insights into the long-term evolution of the East Antarctic Ice Sheet and its glacial–interglacial variability at the western margin of the Ross Embayment.

Here, we build on and refine the interpretation of Lewis and Ashworth (2016) and reconstruct

Figure 13. Glacial–interglacial reconstructions for the Frill Hills region are shown. UTV—upper Taylor Valley; SB—Simmons Basin; FH—Friis Hills; PV—Pearse Valley; MTV—Mid Taylor Valley. Broad regional scale ice-sheet reconstructions from time intervals A–F are based on model simulations from Gasson et al. (2016) and Halberstadt et al. (2021). Surface contours for Friis Hills reconstructions for time intervals A–D are based on geomorphological features in the Pearse Valley and Simmons Basin and ages for similar features in the upper Wright Valley (Lewis et al., 2006). Reconstructed surface contours for maps in time intervals E–F are based on modern topography produced from the Reference Elevation Model of Antarctica (REMA) (<https://www.pgc.umn.edu/data/rema/>) but are inferred to have been lower in elevation in the late middle Miocene. Paleo-elevations shown in cross-section X–X'–X" in panels A–F are reconstructed to accommodate uplift of 300 m that is inferred to have occurred during the middle Miocene Climate Transition and was driven by selective linear erosion and tectonics (see text for details). Paleoglacial flow directions are indicated by blue arrows. Green colors indicate the inferred distribution of vegetation. The blue region in panel F indicates an area at or below 0 m (sea level) that may have been inundated during interglacial marine incursions. Range of $\delta^{18}\text{O}$ values in each reconstruction is based on data from Holbourn et al. (2014) and De Vleeschouwer et al. (2017) as illustrated in Figures 1 and 11.

local paleotopography (Fig. 13) based on key geomorphological features (described below) and surface exposure studies that utilize cosmogenic nuclides and indicate that minimal erosion has occurred at high elevations in the Transantarctic Mountains over the past 15 m.y. (Spectator and Balco, 2021; Valletta et al., 2015). We assume that the floors of the Pearse, Simmonds, and Taylor Valleys that surround the Friis Hills were significantly shallower in the middle Miocene than today (Figs. 13A–13B). We suggest that the U-shaped feature that forms when one connects the platforms at ~1300 m elevation (today) on either side of the Pearse Valley represents the valley floor at ca. 15 Ma (see surface A in cross-sections beneath Figs. 13A–13B). This reconstructed valley floor is at an elevation similar to that of regional surfaces in the Asgard and Olympus Ranges on which other middle Miocene deposits occur (Lewis et al., 2008; Marchant, 1993). Furthermore, this surface occurs at a higher elevation than the Labyrinth and its

East Antarctic Ice Sheet variability during the middle Miocene Climate Transition



geomorphological equivalents (present day ~900 m; surface B in cross-sections beneath Figs. 13C–13D), which formed between 14 Ma and 12 Ma (Lewis et al., 2006). These relationships suggest that surface A represents a regional paleotopography for the early–middle Miocene prior to regional erosion downcutting that produced the modern landscape. We note that seismic reflection data (Brancolini et al., 1995) and glacial-marine sediments in the CIROS-1 (Barrett, 1989) and MSSTS-1 (Barrett, 1986) drill cores at the mouths of the Ferrar and Taylor Valleys indicate that ice flowed down these valleys and episodically extended well beyond the present coastline during the early Miocene.

Friis II drift (lower) sits on surface A and comprises 13 sedimentary cycles deposited by alpine glaciers that advanced and retreated across the central Friis Hills between ca. 15.1 Ma and ca. 14.4 Ma. The first seven glacial–interglacial cycles were deposited during an interval spanning ~170 k.y. (during chron C5Bn.1r) at the end of the MCO. Our temporal constraints indicate that each cycle formed over a ~23 k.y. period and reflects the influence of astronomical precession at the margins of terrestrial ice sheets flowing through the Transantarctic Mountains. Furthermore, our correlation shows that cycles 2 through 6 were deposited between 15 Ma and 14.9 Ma and coincide with a single 100 k.y. eccentricity cycle. Peak warmth and minimum ice volume within this 100 k.y. cycle correlates with a $\delta^{18}\text{O}$ minima (<1.2‰) (Fig. 11C) and occurs during maximum eccentricity (Fig. 11D), both of which coincide with cycles 4 and 5, which comprise relatively thin diamictite units and thick interglacial packages. Intervals of more expansive ice within this eccentricity cycle are recorded in FHDP-3A by relatively thick diamictite packages and thin interglacial units that characterize cycles 2, 3, and 6; coincide with eccentricity minima; and correlate with higher $\delta^{18}\text{O}$ values (>1.4‰).

We infer that disconformity FH-U1 formed during an episode of glacial advance and erosion that coincides with an eccentricity minimum at 14.78 Ma (Fig. 11D) and correlates with a maximum excursion in the $\delta^{18}\text{O}$ record (Fig. 11C). This episode of glacial expansion removed up to 100 k.y. of record from FHDP-3A. Cycles 8–10 capture deposition during progressive warming across three precession cycles within the subsequent 100 k.y. eccentricity cycle. Peak warm environmental conditions and maximum glacial retreat are again captured by the relatively thick interglacial unit of cycle 9. These data show that high-frequency glacial variations at the margin of the East Antarctic Ice Sheet between 15.1 Ma and 14.7 Ma were driven by changes in local insolation paced by astronomical precession.

These high-frequency fluctuations were modulated by short-period eccentricity with peak warmth and maximum glacial retreat during eccentricity maxima.

The onset and early phase of the MMCT (ca. 14.7–14.4 Ma) is recorded in Friis II drift (lower) by a ~250–300 k.y. unconformity (FH-U2) between cycles 10 and 11 (Fig. 11). The coastal sedimentary record through this time interval, captured in the AND-2A drill core, is either missing in an unconformity or comprises thick diamictites that were deposited under a polar glacial regime (Fielding et al., 2011; Levy et al., 2016; Passchier et al., 2011; Fig. 1G). Seismic reflection data from across the Ross Sea also suggest that marine ice sheets advanced and deposited sediment along the outer continental shelf during this time (Colleoni et al., 2018; De Santis et al., 1995, 1999; Pérez et al., 2021). This interval coincides with a period of persistent low eccentricity with muted amplitude variations and includes several glacial episodes during which $\delta^{18}\text{O}$ values exceed 1.8‰ (Fig. 11C). Importantly, this interval is characterized by elevated obliquity sensitivity in $\delta^{18}\text{O}$ data that likely reflects enhanced connection between oceanic processes along the continental margin and Antarctica's ice sheet (Levy et al., 2019). Furthermore, glacial–interglacial cycles recorded by $\delta^{18}\text{O}$ data through this time show clear 40 k.y. cycles paced by changes in obliquity (axial tilt). Together, these data suggest that large, thick outlet glaciers advanced down the Ferrar and Pearse/Taylor Valleys and extended well beyond the coast during glacial maxima (Fig. 13A). Whereas the ice margin may have retreated inland of the Friis Hills during interglacials, subsequent glacial advance and overriding must have eroded any fluvial and lacustrine sediments that accumulated during these warmer episodes.

Cycles 11–13 were deposited between ca. 14.43 Ma and 14.36 Ma and record a short-lived return to environmental change and glacial variability though three precession cycles. These cycles coincide with a relatively unique interval of increasing but moderate short-period eccentricity with muted changes in amplitude. Fluvial and lacustrine units within each cycle show that ice retreated inland from the coast along the shallow and broad paleovalleys to the heads of the Taylor Valley and Simmonds Basin (and possibly further inland) during interglaciations. Despite previous episodes of major glacial expansion (i.e., FH-U2), the Friis Hills still supported an alpine tundra vegetation around a system of small proglacial lakes and bogs linked by fluvial channels to retreated glacier termini (e.g., Fig. 5C).

Significant local environmental change in the Friis Hills occurred between 14.35 Ma and

14.15 Ma, which is reflected by the transition from Friis II drift (lower) to the Friis II drift (upper) that is recorded by a ~200 k.y. disconformity (FH-U3), a shift in character of glacial facies, and a major change in ice-flow direction from 145° to 106° (Lewis and Ashworth, 2016). Sedimentary cycles in Friis II drift (upper) that comprise thick glacial diamictites indicate that the local glaciers that flowed over the site were thicker and more spatially extensive after ca. 14.2 Ma (Lewis and Ashworth, 2016). We infer that these thicker glaciers were fed from expanding ice caps and large outlet glaciers that flowed from the East Antarctic Ice Sheet into the Simmons Basin–Ferrar Valley and Pearse–Middle Taylor Valley during cooler glacial episodes (Fig. 13C). These episodes of major glacial advance in the Friis Hills coincide with an interval where maximum (glacial) values in the $\delta^{18}\text{O}$ record frequently exceed 2‰ (Fig. 11C) and indicate times when extensive but transient marine-based ice sheets once again grew across the Antarctic continental shelf. Glacial erosion increased during this time due to enhanced ice flux (Lewis and Ashworth, 2016), and the Pearse and mid-Taylor Valleys were downcut by at least 300 m, forming a new paleovalley floor at an elevation that corresponded to the Labyrinth surface (see surface B in cross-section below Figs. 13C–13D). Although glacial advances were extensive, large-amplitude, glacial–interglacial climate variability ensured that interglaciations remained relatively warm. Glaciers likely thinned and retreated up valley during these warm interglacial intervals (Fig. 13D).

While chronological control at the top of the Friis Hills sequence is poor, exposure age dating suggests that much of the Friis Hills surface has remained relatively unmodified by erosion since ca. 14 Ma (Valletta et al., 2015). However, deep ocean $\delta^{18}\text{O}$ data indicate that episodes of warm climate and ice-sheet retreat occurred at 14 Ma and ca. 13.9 Ma and coincide with 100 k.y. eccentricity maxima (Fig. 11C). These episodes of relative warmth at the end of the MMCT are reflected in interglacial sediments at the top of FHDP-1A and by fossil assemblages recovered at Mt. Boreas in the Olympus Range (Fig. 2C; Lewis et al., 2008). We note that the network of sinuous channels and potholes cut in bedrock in the upper Pearse Valley, while smaller but similar in appearance to those of the Labyrinth, may have formed at this time during a phase of glacial outburst flooding during the final stages of the MMCT (Lewis et al., 2006). Subsequent glacial advance was larger than during previous events, and by 13.8 Ma, $\delta^{18}\text{O}$ values persistently exceeded 2.2‰ (Fig. 11C).

Immediately after 13.8 Ma, an episode of high-value (cold climate), low-amplitude

variability in deep-sea $\delta^{18}\text{O}$ data (Figs. 1 and 11C) suggests that the AIS “stabilized” at the continental shelf margin and persisted at this position for ~ 150 k.y. This period of maximum marine-based ice extent coincides with a peak in obliquity sensitivity (Levy et al., 2019), a major shift in geochemical weathering signal at DSDP 266 (Vlastelic et al., 2005), and a prominent change in foraminiferal fauna at Ocean Drilling Program (ODP) Hole 747A (Kerguelen Plateau, southern Indian Ocean). Here, taxa with a warm water affinity (e.g., *Globorotalia miozea* group) were replaced by a fauna with typical polar characteristics and dominated by *neoglobotruncanids* (Verducci et al., 2009). Expansion of ice and the transition to a “polar” climate in the Southern Ocean likely contributed to the major perturbation in Southern Ocean phytoplankton at 13.6 Ma (Crampton et al., 2016). Disconformities in the AND-2A record persist through this time, and stacked, mud-poor diamictites indicative of cold polar environments occur at the base of AND-1B (McKay et al., 2009). We infer that enhanced glacial erosion and downcutting during this interval of peak cold and ice extent dissected the “Labyrinth-equivalent” surface in the Pearse Valley and deepened the trunk valleys a further ~ 200 m. Erosion and downcutting in regions south of the Friis Hills reduced ice flow through the Pearse Valley and directed more ice down the Upper Taylor and Ferrar Valleys. The increase in ice flow to the south of the Friis Hills exploited the ever-decreasing elevation of the divide between Friis and Kukri Hills and eventually breached the barrier and flowed into the mid Taylor Valley (Fig. 13C, after Lewis and Ashworth, 2016). The Cavendish Drift was deposited during this interval of “cut and breach” sometime between 13.8 Ma and the late Miocene (Lewis and Ashworth, 2016).

Mud-rich sediments in the AND-2A and AND-1B drill cores indicate that a return from polar conditions to a warmer, sub-polar climate occurred in the early late Miocene (Fielding et al., 2011; McKay et al., 2009; Passchier et al., 2011). Warm water foraminiferal species in the Southern Ocean also increased in abundance after ca. 12.9 Ma (Majewski, 2010; Verducci et al., 2009), which shows that climatic cooling at the termination of the MMCT was transient (Levy et al., 2022). Furthermore, marine diatom fossils recovered from Dry Valley Drilling Project core 4A (Fig. 2C) indicate that the upper Wright Valley was a fjord in the late Miocene (Brady, 1979; Levy et al., 2022; Prentice et al., 1993). These data suggest that the Antarctic Ice Sheet and outlet glaciers in Southern Victoria Land once again retreated inland during interglacial episodes as climate warmed following peak ice-sheet expansion

between 13.8 Ma and ca. 13.6 Ma (Fig. 13F) (Levy et al., 2022). Notwithstanding this, there is no evidence that temperate glaciation or tundra vegetation returned to the Friis Hills or persisted at high elevations in the Transantarctic Mountains after ca. 13 Ma (Lewis et al., 2008, 2007; Marchant, 1993).

CONCLUDING REMARKS

The Friis Hills sedimentary sequence revealed through extensive field work (Lewis and Ashworth, 2016) and the FHDP provides a coherent stratigraphic record of glacial and environmental change in the Transantarctic Mountains from the termination of the MCO through the MMCT. A sedimentary succession of glacial–fluvial–lacustrine facies comprising cycles of diamictite and fossil-rich sandstone and mudstone record relatively short snap shots of glacial advance and retreat across the Central Valley. Radioisotopic and paleomagnetic age constraints allow us to link these sedimentary cycles to astronomical drivers. Our correlations show that glacial–interglacial variability at the terrestrial margin of the East Antarctic Ice Sheet was primarily paced by astronomical precession (~ 23 k.y.) through the onset of the MMCT. These precession-driven cycles were modulated by short-period (~ 100 k.y.) eccentricity. Intervals of maximum eccentricity coincide with precession cycles that comprise thin diamictites and relatively thick sandstone and mudstone packages. Intervals of minimum eccentricity coincide with cycles that include thick diamictites and relatively thin interglacial packages. These relationships suggest that during relatively warm intervals in the early MMCT (ca. 15–14.5 Ma), the East Antarctic Ice Sheet expanded and contracted over 100 k.y. while its margins continued to advance and retreat at higher (~ 23 k.y.) frequency.

Major disconformities spanning more than 100 k.y. in the drill cores occur during intervals of low, long-period eccentricity (400 k.y.) and low-amplitude variability in precession and eccentricity (nodes). These astronomical configurations reduce seasonality, and based on our ice proximal data, they enhance ice-sheet growth. Obliquity is the dominant pacemaker of glacial–interglacial variability in the $\delta^{18}\text{O}$ record after 14.7 Ma. These observations support previous studies that suggest land-terminating Antarctic ice sheets are most sensitive to local insolation forcing paced by precession and modulated by short eccentricity (Galeotti et al., 2016; Levy et al., 2019). The influence of changes in obliquity on the Antarctic Ice Sheet is strongest during times when ice sheets advanced beyond the coast and across the often large continental shelves; their mass balance is

more strongly influenced by obliquity control on ocean forcing (Levy et al., 2019; Naish et al., 2009; Patterson et al., 2014).

This study also reconciles evidence of temperate, alpine-style glaciation in the Friis Hills during the MMCT with evidence of the major advance and retreat of large East Antarctic outlet glaciers through the Transantarctic Mountains into the marine environment along the Southern Victoria Land coast. Selective linear erosion within the large outlet valleys and removal of at least 500 m of bedrock over the past 15 m.y., together with associated isostatic rebound of the Transantarctic Mountains, likely contributed to uplift of the Friis Hills and surrounding mountain ridges, enabling cold and dry polar conditions at higher elevations to dominate following the MMCT. We suggest this provides a mechanism that explains the loss of vegetation at present-day high elevations in the Transantarctic Mountains at ca. 13.8 Ma (Lewis et al., 2008; Lewis and Ashworth, 2016), while sub-polar climatic conditions persisted at the coast through much of the late Miocene and early Pliocene, which supports refugia for higher plants at low elevation coastal locations, such as the Taylor Valley (Fielding et al., 2010; Halberstadt et al., 2021; Ohneiser et al., 2020).

Proxy CO_2 records suggest that average atmospheric concentrations decreased below ~ 400 ppm between 14.8 Ma and 14.6 Ma (Fig. 1B). Major disconformities in the FHDP drill cores, ANDRILL-2A, and IODP U1521, and an increase in Ice Rafted Debris in IODP Site U1356 (Sangiorgi et al., 2018), suggest that major expansion of the East Antarctic Ice Sheet into marine environments coincided with this drop in average CO_2 (Fig. 1F). Deep-sea $\delta^{18}\text{O}$ records also suggest that increased ice volume during glacial episodes occurred after this fall in CO_2 . The FHDP data support previous work and modeling studies indicating that ~ 400 ppm represents a threshold above which Earth’s average climate warms to the point that the Antarctic Ice Sheet cannot sustain marine-based ice sheets (Gasson et al., 2016; Halberstadt et al., 2021; Levy et al., 2016; Naish et al., 2009). Today, CO_2 concentrations are 416 ppm and climbing. We have potentially crossed a key climate threshold, thereby reversing a major cooling step in the Cenozoic evolution of Earth’s climate system that has lasted for ~ 13 m.y.

APPENDIX 1

Here we provide a detailed description of each lithofacies and its environmental interpretation, which form the building blocks of a sequence stratigraphic interpretation (Figs. 3–4) and outline a depositional model (Fig. 5) for the recurrent advance and retreat of

a mountain glacier system in the Friis Hills during the middle Miocene.

Facies 1—Mudstone and fine-sandy mudstone

Description

Light-brown to dark-olive-brown, organic-rich, massive to horizontally stratified, laminated and bedded, mudstone and fine, sandy mudstone with dispersed extraformational clasts of dolerite and granite (Figs. 6A–6B). Stratification is expressed by bedding of up to 1.5 cm thick and sub-millimeter-scale laminae of siltstone or very fine sandstone; however, stratification is highly disturbed near erosional contacts (GSEs; Fig. 6B). This facies is organic-rich, with total organic carbon comprising up to 13.27%. Organic material is fine-grained and disseminated, with some macrofossils of woody material, leaves, moss mats, and seeds. Palynomorphs include pollen, spores, and *Botryococcus*, an algae that is characteristic of freshwater environments. Siliceous microfossils are commonly present (in 18 out of 23 samples) and include freshwater diatoms such as *Staurosirella* spp., *Staurosira* spp., and cysts of Chrysophycean flagellates. This facies commonly preserves soft-sediment deformation structures in discrete intervals, as convolute bedding and folding, sedimentary intrusions (clastic sills and dykes, with fills of mud, sand, or diamictite), and load structures, especially when it occurs stratigraphically below a GSE (Figs. 6A–6B). Additionally, brittle deformation is expressed by mineralized fractures, micro-faults, high-angle reverse faults, and low-angle thrusts concordant with bedding, physical mixing/shearing, as well as brecciation. Some brittle deformation features cross-cut soft-sediment deformation features. Occasional extraformational clasts of dolerite and granite are dispersed within the mudstone, and concentrations tend to increase toward the top. These dispersed clasts are often associated with sag and drape features.

Interpretation

Facies 1 represents the lowest energy and most ice-distal deposits in the Friis Hills sediment cores and consists of hemipelagic sediments. The lack of bioturbation, high organic matter content, and rare to abundant organic macrofossils with freshwater diatoms indicate a lacustrine setting (Fitzsimons, 1992). The dominant diatom in several samples (>80% in 5 out of 18 diatomaceous samples) is a *Staurosirella* spp., which occurs in alpine lakes with benign turbulence and low water turnover (Rimet et al., 2019). The occasional occurrence of rare, dispersed sub-angular to sub-rounded extraformational clasts and associated sag and drape features indicates deposition from episodic iceberg rafting from a lake-terminating glacier. The occurrence of subtle horizontal stratification may represent episodic and seasonal to sub-seasonal fluctuations in meltwater/sediment discharge and/or lake ice (varves). The latter form occurs as wind-blown fine sand and is released to the lake floor as lake ice melts. Convolute bedding and slump features may represent the effects of downslope instability from small seismic events, sediment overloading or glaci-tectonics. Intraformational, soft-sediment lenses and brittle deformation, with an increased abundance of coarse material (clasts >2 mm), indicate iceberg rafting, and they typically occur where facies 1 immediately underlies a sharp-based diamictite and is interpreted as subglacial deformation associated with subsequent ice advance, grounding, and overriding in a pro-glacial lacustrine environment (van der Meer and Menzies, 2011). Brittle deformation and fractures, cross-cutting folded and convolute soft-sediments, and vertically

fractured limestones imply post-depositional ice overriding of this lacustrine facies (Hiemstra and van der Meer, 1997).

Facies 2—Interstratified mudstone and sandstone

Description

Gray to brown, laminated and bedded (up to 5 cm thick), carbonaceous, horizontally interstratified mudstone and fine sandstone with dispersed extraclasts of dolerite and granite (Figs. 6C–6E). Unlike facies 1, stratification is generally moderate to strong and is defined by up to 5-cm-thick units of brown, laminated mudstone or normally graded, sandy fine mudstone and fine grained sandstone (Figs. 6D–6E). Organic material is fine-grained and disseminated, but occasional macrofossils of woody material, leaves, moss mats, and seeds are present. This facies generally contains less organic material than facies 1; however, some samples have up to 11.77% total organic carbon. Freshwater diatoms are often present (in 15 out of 23 samples), with *Eunotia* the most common genus in seven out of 15 diatomaceous samples. Soft-sediment deformational structures occur in discrete intervals and include convolute bedding and folding (Figs. 6D–6E), sedimentary intrusions (such as clastic sills and dykes with fills of mud, sand, or diamictite) (Fig. 6C), and load structures. Very rare feather fragments are observed in some samples. Brittle deformation is expressed by mineralized fractures, high-angle reverse microfaults (Fig. 6E), physical mixing/shearing as well as brecciation, and occasional limestones (Figs. 6C–6E). Some brittle deformation features cross-cut soft-sediment deformation features. Deformation is more pervasive in this facies than in facies 1.

Interpretation

Facies 2 represents subaqueous depositional conditions in which sand supply was greater than in facies 1 and is interpreted to have formed in a shallow, ice-proximal, proglacial lacustrine environment. The thinly interbedded nature of the facies suggests quiescent conditions where fine sediment settled out of suspension for much of the time was episodically punctuated by short, discrete events during which coarse sediment was deposited. During these events, sand was deposited rapidly from decelerating flows, perhaps at the base of a subaqueous fan receiving glacial outwash sand from a subglacial fluvial conduit or via a fluvial delta system in the proglacial environment (McCabe and Eyles, 1988; Walker and James, 1992). The presence of *Eunotia* spp. diatoms that live attached to stones or waterweeds and prefer humic (peaty) water (Wolfe, 1994) indicates more fluvial input than in facies 1. The occurrence of normally graded units and intraclast breccias implies an unstable sloping substrate, but not steep or high-energy enough to deliver reverse-graded deposits of coarse sediment. The lack of gravel and the relative thinness of the units (<5 cm) implies a shoreline-distal setting and/or a relatively small delta in a small lake. The relatively pervasive occurrence of both brittle and ductile deformation features suggests a more proximal glacial depositional setting and is interpreted as a combination of syn-depositional slumping and post-depositional deformation due to subsequent glacial overriding (van der Meer, 1993).

Facies 3—Graded sandstone

Description

Dark-gray to olive and light-gray, normally graded beds of up to 30 cm thick, which contain poorly sorted,

pebbly coarse sandstone that fines upwards into well-sorted, laminated fine sandstone (Fig. 6F). Facies 3 includes graded-sandstone beds that are like facies 2 but lack hemipelagic mudstone beds that commonly sit above sandstone beds in facies 2. Pebby sandstones are sharp-based and truncate underlying laminated fine sandstones, which may be low-angle cross or convolute bedded. Pebble clasts are angular to sub-rounded. This facies contains intervals of convolute folded and sheared, physically intermixed strata.

Interpretation

Vertical amalgamation of up to 12 normally graded sandstone beds between 28.40 m and 40.00 m in FHDP-3A (Fig. 6F) implies rapid deposition by sediment gravity flows on a delta front or toe in a more shoreline proximal environment than that of facies 2. Convex-upwards and convolute lamination in the top of each graded unit is consistent with the settling of fine sand out of a turbid plume under declining flow, such as in a turbidite. These features also resemble hummocky cross-stratification deposited as a result of declining return flow from storm surge (Plint, 1988; Walker and James, 1992). However, the lack of mud and the normally graded nature of this facies are more consistent with a non-cohesive and subaqueous debris flow (Nemec, 1990; Postma, 1986), such as grain-flows (Nemec and Steel, 1984). The lack of outsized clasts in laminated sandstones indicates limited or no occurrence of iceberg rafting, which suggests the time between deposition of successive units was short and/or the glacier was land-terminating with a river/stream delivering well-sorted sand to a small, fluvial-lacustrine delta (Fielding, 1984; Horton and Schmitt, 1996; Tye and Coleman, 1989; Walker and James, 1992).

Facies 4—Sandstone

Description

Gray to yellow-brown massive to horizontally bedded (up to 30-cm-thick), moderately to poorly sorted, muddy-fine to pebbly coarse sandstone (Fig. 6G). Varieties of poorly sorted, mud-rich, fine- to coarse-grained sandstones generally lacking internal sedimentary structure characterize facies 4. Thin mudstone (facies 1) intervals of up to 3 cm thick separate many of the sand beds (Fig. 6G). Sedimentary structure is poorly developed, and horizontal stratification is often weak and defined by intervening mud beds with no evidence of tractional deposition by currents. Some beds are normally graded and may represent variants on facies 2 and 3 with sharp and sometimes erosive lower contacts. Many of the beds include extraformational mud clasts “floating” within a muddy sand matrix, whereas in a few cases concentrations of clasts occur either at the base or at the top of beds. Soft-sediment deformation structures were noted only locally. Diatoms are sometimes present in the various sandstone facies (present in 15 out of 25 samples), with *Staurosirella* spp. and cysts of Chrysophycean flagellates most common. Very rare feather fragments are observed in some samples.

Interpretation

The mud-rich, poorly sorted, and unstratified nature of facies 4 is suggestive of sediment deposition from sandy sediment gravity flows. The lack of sedimentary structures resembles a subaqueous, cohesive debris flow, such as a hyperconcentrated flow. Moreover, the occurrence of floating extraformational clasts and rip-ups is characteristic of a debris flow (Shanmugam, 1996), which reflects the mass transport and

rapid deposition of these sediments (Benn and Evans, 2010). The occurrence of facies 4 in association with facies 2 and 3 is consistent with deposition in delta front or delta toe lacustrine environments. No direct evidence of glacial conditions can be inferred from facies 4, although the debris flows could have originated near a lake-terminating glacier.

Facies 5—Cross-stratified sandstone

Description

Yellow-brown to gray, well-sorted, cross-stratified fine to coarse sandstone (Figs. 6H–6I). Facies 5 comprises stratified (millimeter- to centimeter-scale) sandstone beds that coarsen upwards and exhibit ripple cross-bedding with steep angle, centimeter-scale cross-bedding (Figs. 6H and 6I). Fine to coarse sandstone intervals and pebble nests often separate beds, and mud drapes occur on low-angle ripples. Stratification is often well-defined, however weak stratification occurs within more physically intermixed units. In general, the lower contact of facies 5 is gradational, with high-angle erosional surfaces of the underlying facies also associated with those units that are physically intermixed. In most cases, facies 5 shows far less deformation than facies 1–4. Rare limestones occur toward the upper section of each unit (Fig. 6H). Very rare feather fragments are observed in some samples.

Interpretation

Coarsening-upward successions of cross-bedded sands such as those that occur in facies 5 are common in prograding deltas (Eyles and Eyles, 1983). Assemblages of laminated, cross-stratified, ripple- and cross-bedded sands are also indicative of shoreline-distal sedimentation (Thomas et al., 2004). Ripple cross-bedding is particularly common in sandy fluvial and glacio-lacustrine environments (Benn and Evans, 2010), whereas a lack of ice rafted debris in some sequences suggests accumulation in a prograding delta in water sufficiently shallow to exclude large icebergs (Porter and Beget, 1981). Mud drapes likely formed as flows waned and fine, suspended sediment settled out of stagnant water left in abandoned channels (Miall, 1977). Where facies 5 is truncated by a glacial surface of erosion and is physically intermixed with the underlying facies, deposition may have occurred in a subglacial fluvial channel.

Facies 6—Breccia

Description

Light olive-brown, clast-rich, poorly sorted breccia with a muddy sand matrix. Clasts are angular to sub-rounded and dominated by intraclasts and clastic intrusions derived from underlying sediments. This facies is rare, but where it occurs it coincides with the GSE at the base of a massive diamictite (facies 8). It is generally deformed and displays physical intermixing.

Interpretation

Redeposition of previously deposited sediments by mass flows including rip-ups, physical intermixing, and shearing, along with close association with facies 8, suggest that facies 7 is a glaciectonite (Atkins et al., 2002) and most likely represents the lowermost layer in a traction till that was produced as sediments were sheared beneath overriding ice. Fine-grained sediments can be heavily deformed in this environment, but coarser units such as sands or gravels form

relatively undeformed pods or lenses in response to ice over-riding (Benn and Evans, 2010).

Facies 7—Stratified diamictite

Description

Gray, clast-rich to clast-poor, sandy or muddy sub-horizontal to high-angle, weakly stratified (beds of up to 20 cm thick) diamictite (Fig. 6J). This facies is relatively uncommon in the Friis Hills sediments but does occur throughout FHDP-3A and upper parts of FHDP-1A, where it sits above massive diamictite. Stratified diamictites grade into and out of massive diamictite facies but generally occur above massive diamictites at the transition to glacio-fluvial or lacustrine proglacial facies (facies 1–5). Centimeter-scale stratification is defined by concentrations of angular to sub-rounded clasts with increased sand matrix that is separated by fine, sandy mudstone beds (Fig. 6J). In some cases, clasts are aligned along the a-axis parallel to bedding, which resembles imbrication.

Interpretation

Stratified diamictites with low clast counts most likely formed as cohesive debris flows with sufficient melt water to concentrate clasts, whereas clast alignment is likely related to melt-out processes (Lawson, 1979). Deformation structures suggest that subaerial deposition of this facies is most likely as these structures probably formed as sediment was deposited by collapsing ice at the margin of melting glaciers (Fitzsimons, 1992).

Facies 8—Massive diamictite

Description

Gray to yellow-brown, massive clast-rich to clast-poor, sandy to intermediate diamictite (Fig. 7) is the most common facies in the Friis Hills cores. Diamictite units vary from 0.2 m to 13.3 m in thickness. Grain-size distributions of the matrix are typically broad but generally follow a polymodal distribution (Table S1). There is an overall trend of a gradual fining upwards of the matrix through each of the diamictite successions. The mud content of the matrix varies from 23% to 93% throughout the core. Clasts are randomly oriented and range from angular (Fig. 7D) to subrounded (Fig. 7H), and many are striated and faceted. Some display vertical fractures (Figs. 7A, 7C, 7F, and 7H), rotational features (Figs. 7B and 7E), clast halos (Figs. 7B and 7E), and mud-filled faults (Fig. 7F). In some intervals, the matrix fabric is sheared (Figs. 7D and 7I), and/or fractured, and/or displays necking and comet structures (Fig. 7E). Porewater escape features, shear zones (Fig. 7I), and layering and foliation features are also evident.

These deformation features tend to be concentrated in the lower portions of diamictite units, where the basal contact is often sharp, erosional, and exhibits load features. Immediately underlying lithologies, commonly comprising facies 1, 2, and 3, display a range of ductile and brittle deformation features. The basal parts of this facies often include extraclast (rip-ups) of underlying lithologies (Fig. 7G), clastic sills and dykes (Fig. 7D), and pebbly, coarse sands that are physically intermixed with underlying lithologies. Pods of gravel and sand-sized clasts of up to 0.5 cm occur intermittently. These features are structureless, but some are deformed by overlying sediment. The upper portions of this facies are typically less

deformed, but the texture remains equally homogenized. Diamictites in the upper part of FHDP-1A and FHDP-2A tend to be lighter in color compared to the lower intervals of FHDP-2A and all of FHDP-3A (see Supplemental Material). Lewis and Ashworth (2016) also note this distinct color change between the Friis II lower and upper drifts.

Interpretation

Sharp-based, massive, structureless diamictites, which dominate this facies, are interpreted broadly as subglacial traction tills (Benn and Evans, 2010; Evans et al., 2006). At a sequence stratigraphic scale, this facies often overlies proglacial fluvio-lacustrine mudstone, sandstone, and gravel facies (1–5), which display a range of ductile and brittle deformation features consistent with shearing and compressional loading (van der Meer, 1993). Ductile deformation in the lower portions of this facies expressed as physical intermixing of underlying lithologies, clastic intrusions, comet structures, and lee-side cavity-fills, folding and crenulation, and matrix realignment are consistent with shearing and loading by sliding, overriding ice (van der Meer, 1993). Additionally, faceted and striated clasts with strain caps and evidence of rotation, and bi-modal grain-size distributions in the matrix, imply processes of subglacial transport in lodgement tills (van der Meer, 1993).

Facies 9—Tephra

Description

White/gray, deformed, massive to laminated, vitric, sandy to silty mudstone (tephra) of up to 20 cm thick. Laminations occur on the millimeter and centimeter scale, with intercalated limestones ranging in size from 2 mm to 5 cm. Tephra in the FHDP cores are fortuitously preserved beneath GSEs and are physically intermixed and deformed locally as pods and intraclasts of volcanioclastic sediment (Figs. 8A–8C). Lower contacts of the tephra layers are generally sharp and irregular, whereas the upper contacts tend to be gradational and usually contain an admixture of ash and terrigenous grains disseminated over millimeters to centimeters.

Interpretation

The tephra are interpreted as the products of primary volcanic air-fall processes and subsequent remobilization within fluvio-lacustrine sedimentary environments during interglacial episodes. The tephra at 5.3 m in FHDP-2A is rhyolitic, and the tephra at 27.2 m in FHDP-3A is trachytic (Fig. 9A). The rhyolitic tephra in FHDP-2A contains two distinct glass populations based on major element analysis (Figs. 9A–9B). Mixed glass populations may result from a variety of origins, including post-emplacement sedimentary reworking of different eruptive deposits, or eruption of a chemically zoned magma chamber, and therefore, a minimum age of emplacement can be determined. FHDP-3A contains a single, tightly clustered glass composition consistent with a single eruptive event. The Mount Morning volcanic center (Fig. 2) is the likely source of the tephra in FHDP-2A and FHDP-3A as both trachytic and rhyolitic features formed within this center during the middle Miocene (Martin et al., 2010).

ACKNOWLEDGMENTS

We thank Alex Pyne, who developed the drilling methodology to recover core in a challenging

environment. Thanks also go to Tony Kingan and Adam Rutland for their efforts to get us into the field and operate the drilling system and to the team at Webster Drilling and Exploration for its support and enthusiasm for scientific drilling in Antarctica. We thank Rebecca Pyne, who helped curate and manage the core both in the field and at the core facility at GNS Science, Wellington, New Zealand. The staff at Antarctica New Zealand are thanked for their excellent support in getting us to and from the field. Special thanks go to Andrew Hefford from Southern Lakes Helicopters for safely moving the drilling system between the drilling sites. Funding support was provided by the New Zealand Ministry of Business, Innovation and Employment through the Past Antarctic Science Programme (C05X1001); Antarctic Science Platform (ANTA1801); and the National Science Foundation (1638954). Hannah Chorley was funded by a Victoria University of Wellington doctoral scholarship.

REFERENCES CITED

- Ashworth, A.C., and Cantrill, D.J., 2004, Neogene vegetation of the Meyer Desert Formation (Sirius Group) Transantarctic Mountains, Antarctica: Palaeogeography, Palaeoclimatology, Palaeoecology, v. 213, p. 65–82, [https://doi.org/10.1016/S0031-0182\(04\)00359-1](https://doi.org/10.1016/S0031-0182(04)00359-1).
- Askin, R., 1995, Permian palynomorphs from southern Victoria Land, Antarctica: *Antarctic Journal of the United States*, v. 30, p. 47–47.
- Askin, R.A., 2000, Spores and pollen from the McMurdo Sound erratics, Antarctica, in Stilwell, J.D., and Feldmann, R.M., eds., *Paleobiology and Paleoenvironments of Eocene Fossiliferous Erratics, McMurdo Sound, East Antarctica*. Washington, D.C., American Geophysical Union, Antarctic Research Series, v. 76, p. 161–181, <https://doi.org/10.1029/AR076p0161>.
- Askin, R.A., and Raine, J.I., 2000, Oligocene and early Miocene terrestrial Palynology of CRP-2/2A, Victoria Land Basin, Antarctica: *Terra Antarctica*, v. 7, no. 4–5, p. 493–501.
- Atkins, C.B., Barrett, P.J., and Hicock, S.R., 2002, Cold glaciers erode and deposit; evidence from Allan Hills, Antarctica: *Geology*, v. 30, no. 7, p. 659–662, [https://doi.org/10.1130/0091-7613\(2002\)030<0659:CGDE>2.0.CO;2](https://doi.org/10.1130/0091-7613(2002)030<0659:CGDE>2.0.CO;2).
- Badger, M.P.S., Lear, C.H., Pancost, R.D., Foster, G.L., Bailey, T.R., Leng, M.J., and Abels, H.A., 2013, CO₂ drawdown following the middle Miocene expansion of the Antarctic Ice Sheet: *Paleoceanography*, v. 28, no. 1, p. 42–53, <https://doi.org/10.1002/palo.20015>.
- Barrett, P.J., 1986, Antarctic Cenozoic history from the MSSTS-1 drillhole, McMurdo Sound: *DSIR Bulletin*, v. 237, p. 172.
- Barrett, P.J., ed., 1989, Antarctic Cenozoic history from CIROS-1 drillhole, McMurdo Sound: *DSIR Bulletin*, v. 245, p. 241–251.
- Bearling, D.J., Fox, A., and Anderson, C.W., 2009, Quantitative uncertainty analyses of ancient atmospheric CO₂ estimates from fossil leaves: *American Journal of Science*, v. 309, no. 9, p. 775–787, <https://doi.org/10.2475/09.2009.01>.
- Benn, D., and Evans, D., 1998, *Glaciers and Glaciation*, 1st ed.: Arnold.
- Benn, D., and Evans, D., 2010, *Glaciers and Glaciation*: London, Hodder Education, 802 p.
- Bennett, M., Huddart, D., and McCormick, T., 2000, The Glaciolacustrine Landform–Sediment Assemblage at Heinabergsjökull, Iceland: *Geografiska Annaler. Series A. Physical Geography*, v. 82, no. 1, p. 1–16, <https://doi.org/10.1111/j.0435-3676.2000.00107.x>.
- Böhme, M., 2003, The Miocene climatic optimum: Evidence from ectothermic vertebrates of Central Europe: *Palaeogeography, Palaeoclimatology, Palaeoecology*, v. 195, no. 3–4, p. 389–401, [https://doi.org/10.1016/S0031-0182\(03\)00367-5](https://doi.org/10.1016/S0031-0182(03)00367-5).
- Bolton, C.T., Hernández-Sánchez, M.T., Fuertes, M.-Á., González-Lemos, S., Abrevaya, L., Mendez-Vicente, A., Flores, J.-A., Probert, I., Giosan, L., Johnson, J., and Stoll, H.M., 2016, Decrease in coccolithophore calcification and CO₂ since the middle Miocene: *Nature Communications*, v. 7, no. 1, <https://doi.org/10.1038/ncomms10284>.
- Brady, H.T., 1979, A Diatom report on DVDP cores 3, 4A, 12, 14, 15 and other related surface sections: *Memoirs of National Institute of Polar Research*, v. 13, p. 165–175.
- Brancolini, G., Cooper, A.K., Coren, F., 1995, Seismic facies and glacial history in the western Ross Sea (Antarctica), in Cooper, A.K., Barker, P.F., and Brancolini, G., eds., *Geology and Seismic Stratigraphy of the Antarctic Margin: Antarctic Research Series*, v. 68, p. 209–233, <https://doi.org/10.1029/AR068p0209>.
- Cerling, T.E., 1992, Use of carbon isotopes in paleosols as an indicator of the P(CO₂) of the paleoatmosphere: *Global Biogeochemical Cycles*, v. 6, no. 3, p. 307–314, <https://doi.org/10.1029/92GB01102>.
- Clapperton, C.M., and Sugden, D.E., 1990, Late Cenozoic glacial history of the Ross Embayment, Antarctica: *Quaternary Science Reviews*, v. 9, no. 2–3, p. 253–272, [https://doi.org/10.1016/0277-3791\(90\)90021-2](https://doi.org/10.1016/0277-3791(90)90021-2).
- Colleoni, F., De Santis, L., Siddoway, C.S., Bergamasco, A., Golledge, N.R., Lohmann, G., Passchier, S., and Siegert, M.J., 2018, Spatio-temporal variability of processes across Antarctic ice-bed–ocean interfaces: *Nature Communications*, v. 9, 2289, <https://doi.org/10.1038/s41467-018-04583-0>.
- Coxall, H.K., Wilson, P.A., Páliké, H., Lear, C.H., and Backman, J., 2005, Rapid stepwise onset of Antarctic glaciation and deeper calcite compensation in the Pacific Ocean: *Nature*, v. 433, p. 53–57, <https://doi.org/10.1038/nature03135>.
- Cramer, B.S., Miller, K.G., Barrett, P.J., and Wright, J.D., 2011, Late Cretaceous–Neogene trends in deep ocean temperature and continental ice volume: Reconciling records of benthic foraminiferal geochemistry (^δ¹⁸O and Mg/Ca) with sea level history: *Journal of Geophysical Research: Oceans*, v. 116, no. C12, C12023, <https://doi.org/10.1029/2011JC007255>.
- Crampton, J.S., Cody, R.D., Levy, R., Harwood, D., McKay, R., and Naish, T.R., 2016, Southern Ocean phytoplankton turnover in response to stepwise Antarctic cooling over the past 15 million years: *Proceedings of the National Academy of Sciences of the United States of America*, v. 113, no. 25, p. 6868–6873, <https://doi.org/10.1073/pnas.1600318113>.
- De Santis, L., Anderson, J.B., Brancolini, G., and Zayatz, I., 1995, Seismic record of Late Oligocene through Miocene glaciation on the central and eastern continental shelf of the Ross Sea, in Cooper, A.K., et al., eds., *Geology and Seismic Stratigraphy of the Antarctic Margin: Washington, D.C.*, American Geophysical Union, Antarctic Research Series, v. 68, p. 235–260, <https://doi.org/10.1029/AR068p0235>.
- De Santis, L., Prato, S., Brancolini, G., Lovo, M., and Torelli, L., 1999, The Eastern Ross Sea continental shelf during the Cenozoic: implications for the West Antarctic ice sheet development: *Global and Planetary Change*, v. 23, no. 1–4, p. 173–196, [https://doi.org/10.1016/S0921-8181\(99\)00056-9](https://doi.org/10.1016/S0921-8181(99)00056-9).
- De Vleeschouwer, D., Vahlenkamp, M., Crucifix, M., and Páliké, H., 2017, Alternating Southern and Northern Hemisphere climate response to astronomical forcing during the past 35 m.y.: *Geology*, v. 45, no. 4, p. 375–378, <https://doi.org/10.1130/G38663.1>.
- Dunbar, G.B., Naish, T.R., Barrett, P.J., Fielding, C.R., and Powell, R.D., 2008, Constraining the amplitude of late Oligocene bathymetric changes in Western Ross Sea during orbitally-induced oscillations in the East Antarctic Ice Sheet: (1) Implications for glaciomarine sequence stratigraphic models: *Palaeogeography, Palaeoclimatology, Palaeoecology*, v. 260, p. 50–65, <https://doi.org/10.1016/j.palaeo.2007.08.018>.
- Ekart, D.D., Cerling, T.E., Montanez, I.P., and Tabor, N.J., 1999, A 400 million year carbon isotope record of pedogenic carbonate; implications for paleoatmospheric carbon dioxide: *American Journal of Science*, v. 299, no. 10, p. 805–827, <https://doi.org/10.2475/aj.s.299.10.805>.
- Evans, D., Phillips, E., Hiemstra, J., and Auton, C., 2006, Subglacial till: Formation, sedimentary characteristics and classification: *Earth-Science Reviews*, v. 78, no. 1–2, p. 115–176, <https://doi.org/10.1016/j.earscirev.2006.04.001>.
- Eyles, C.H., and Eyles, N., 1983, Sedimentation in a large lake: A reinterpretation of the late Pleistocene stratigraphy at Scarborough Bluffs, Ontario, Canada: *Geology*, v. 11, no. 3, p. 146–152, [https://doi.org/10.1130/0091-7613\(1983\)11<146:SIALLA>2.0.CO;2](https://doi.org/10.1130/0091-7613(1983)11<146:SIALLA>2.0.CO;2).
- Eyles, N., Sladen, J.A., and Gilro, S., 1982, A depositional model for stratigraphic complexes and facies superimposition in lodgement tills: *Boreas*, v. 11, no. 4, p. 317–333, <https://doi.org/10.1111/j.1502-3885.1982.tb00541.x>.
- Eyles, N., Clark, B.M., and Clague, J.J., 1987, Coarse-grained sediment gravity flow facies in a large supraglacial lake: *Sedimentology*, v. 34, no. 2, p. 193–216, <https://doi.org/10.1111/j.1365-3091.1987.tb00771.x>.
- Fielding, C.R., 1984, Upper delta plain lacustrine and fluviolacustrine facies from the Westphalian of the Durham Coalfield, NE England: *Sedimentology*, v. 31, no. 4, p. 547–567, <https://doi.org/10.1111/j.1365-3091.1984.tb01819.x>.
- Fielding, C.R., Browne, G.H., Field, B., Florindo, F., Harwood, D.M., Krissie, L.A., Levy, R.H., Panter, K.S., Passchier, S., and Pekar, S.F., 2011, Sequence stratigraphy of the ANDRILL AND-2A drillcore, Antarctica: A long-term, ice-proximal record of early to mid-Miocene climate, sea-level and glacial dynamism: *Palaeogeography, Palaeoclimatology, Palaeoecology*, v. 305, no. 1–4, p. 337–351, <https://doi.org/10.1016/j.palaeo.2011.03.026>.
- Fielding, C.R., Harwood, D.M., Winter, D.M., and Francis, J.E., 2012, Neogene stratigraphy of Taylor Valley, Transantarctic Mountains, Antarctica: evidence for climate dynamism and a vegetated early Pliocene coastline of McMurdo Sound: *Global and Planetary Change*, v. 96, p. 97–104, <https://doi.org/10.1016/j.gloplacha.2010.09.003>.
- Fitzsimons, S.J., 1992, Sedimentology and depositional model for glaciolacustrine deposits in an ice-dammed tributary valley, western Tasmania, Australia: *Sedimentology*, v. 39, no. 3, p. 393–410, <https://doi.org/10.1111/j.1365-3091.1992.tb02124.x>.
- Florindo, F., Wilson, G.S., Roberts, A.P., Sagnotti, L., and Verosub, K.L., 2005, Magnetostratigraphic chronology of a late Eocene to early Miocene glaciomarine succession from the Victoria Land Basin, Ross Sea, Antarctica: *Global and Planetary Change*, v. 45, no. 1–3, p. 207–236, <https://doi.org/10.1016/j.gloplacha.2004.09.009>.
- Flower, B.P., and Kennett, J.P., 1993, Middle Miocene ocean-climate transition: High-resolution oxygen and carbon isotopic records from Deep Sea Drilling Project Site 588A, southwest Pacific: *Paleoceanography*, v. 8, no. 6, p. 811–843, <https://doi.org/10.1029/93PA02196>.
- Flower, B.P., and Kennett, J.P., 1994, The middle Miocene climatic transition: East Antarctic ice sheet development, deep ocean circulation and global carbon cycling: *Palaeogeography, Palaeoclimatology, Palaeoecology*, v. 108, no. 3–4, p. 537–555, [https://doi.org/10.1016/0031-0182\(94\)90251-8](https://doi.org/10.1016/0031-0182(94)90251-8).
- Foster, G.L., and Rohling, E.J., 2013, Relationship between sea level and climate forcing by CO₂ on geological timescales: *Proceedings of the National Academy of Sciences of the United States of America*, v. 110, no. 4, p. 1209–1214, <https://doi.org/10.1073/pnas.1216073110>.
- Foster, G.L., Lear, C.H., and Rae, J.W.B., 2012, The evolution of pCO₂, ice volume and climate during the middle Miocene: *Earth and Planetary Science Letters*, v. 341–344, p. 243–254, <https://doi.org/10.1016/j.epsl.2012.06.007>.
- Galeotti, S., DeConto, R., Naish, T., Stocchi, P., Florindo, F., Pagani, M., Barrett, P., Bohaty, S.M., Lanci, L., Pollard, D., Sandroni, S., Talarico, F.M., and Zachos, J.C., 2016, Antarctic Ice Sheet variability across the Eocene–Oligocene boundary climate transition: *Science*, v. 352, no. 6281, p. 76–80, <https://doi.org/10.1126/science.aab0669>.
- Gasson, E., DeConto, R.M., Pollard, D., and Levy, R.H., 2016, Dynamic Antarctic ice sheet during the early to mid-Miocene: *Proceedings of the National Academy of Sciences of the United States of America*, v. 113, no. 13, p. 3459–3464, <https://doi.org/10.1073/pnas.1516130113>.

- Gradstein, F.M., and Ogg, J.G., 2020, The Chronostratigraphic Scale, in Gradstein, F.M., Ogg, J.G., Schmitz, M.D., and Ogg, G.M., eds., Geologic Time Scale 2020: Amsterdam, Elsevier, p. 21–32, <https://doi.org/10.1016/B978-0-12-824360-2.00002-4>.
- Greenop, R., Foster, G.L., Wilson, P.A., and Lear, C.H., 2014, Middle Miocene climate instability associated with high-amplitude CO₂ variability: Paleoceanography, v. 29, p. 845–853, <https://doi.org/10.1002/2014PA002653>.
- Halberstadt, A.R.W., Chorley, H., Levy, R.H., Naish, T., DeConto, R.M., Gasson, E., and Kowalewski, D.E., 2021, CO₂ and tectonic controls on Antarctic climate and ice-sheet evolution in the mid-Miocene: Earth and Planetary Science Letters, v. 564, <https://doi.org/10.1016/j.epsl.2021.116908>.
- Hart, J.K., 1996, Proglacial glaciectonic deformation associated with glaciolacustrine sedimentation, Lake Pukaki, New Zealand: Journal of Quaternary Science, v. 11, no. 2, p. 149–160, [https://doi.org/10.1002/\(SICI\)1099-1417\(199603/04\)11:2<149::AID-JQS227>3.0.CO;2-2](https://doi.org/10.1002/(SICI)1099-1417(199603/04)11:2<149::AID-JQS227>3.0.CO;2-2).
- Hart, J.K., and Boulton, G.S., 1991, The interrelation of glaciectonic and glaciodepositional processes within the glacial environment: Quaternary Science Reviews, v. 10, no. 4, p. 335–350, [https://doi.org/10.1016/0277-3791\(91\)90035-S](https://doi.org/10.1016/0277-3791(91)90035-S).
- Hart, J.K., and Peglar, S.M., 1990, Further evidence for the timing of the Middle Pleistocene glaciation in Britain: Proceedings of the Geologists' Association, v. 101, no. 3, p. 187–196.
- Herold, N., Muller, R.D., and Seton, M., 2010, Comparing early to middle Miocene terrestrial climate simulations with geological data: Geosphere, v. 6, no. 6, p. 952–961, <https://doi.org/10.1130/GES00544.1>.
- Hiemstra, J.F., and van der Meer, J.J.M., 1997, Pore-water controlled grain fracturing as indicator for subglacial shearing in till: Journal of Glaciology, v. 43, no. 145, p. 446–454, <https://doi.org/10.1017/S0022143000035036>.
- Ho, S.L., and Laepple, T., 2016, Flat meridional temperature gradient in the early Eocene in the subsurface rather than surface ocean: Nature Geoscience, v. 9, no. 8, p. 606–610, <https://doi.org/10.1038/geo2763>.
- Holbourn, A., Kuhnt, W., Lyle, M., Schneider, L., Romero, O., and Andersen, N., 2014, Middle Miocene climate cooling linked to intensification of eastern equatorial Pacific upwelling: Geology, v. 42, no. 1, p. 19–22, <https://doi.org/10.1130/G34890.1>.
- Horton, B.K., and Schmitt, J.G., 1996, Sedimentology of a lacustrine fan-delta system, Miocene Horse Camp Formation, Nevada, USA: Sedimentology, v. 43, no. 1, p. 133–155, <https://doi.org/10.1111/j.1365-3091.1996.tb01464.x>.
- IPCC, 2013, Climate Change 2013: The Physical Science Basis, in Contribution of Working Group 1 to the Fifth Assessment Report Intergovernmental Panel on Climate Change: Cambridge, UK, Cambridge University Press, 1552 p.
- Ji, S., Nie, J., Lechner, A., Huntington, K.W., Heitmann, E.O., and Breecker, D.O., 2018, A symmetrical CO₂ peak and asymmetrical climate change during the middle Miocene: Earth and Planetary Science Letters, v. 499, p. 134–144, <https://doi.org/10.1016/j.epsl.2018.07.011>.
- John, C.M., Karner, G.D., Browning, E., Leckie, R.M., Matteo, Z., Carson, B., and Lowery, C., 2011, Timing and magnitude of Miocene eustasy derived from the mixed siliciclastic-carbonate stratigraphic record of the northeastern Australian margin: Earth and Planetary Science Letters, v. 304, no. 3–4, p. 455–467, <https://doi.org/10.1016/j.epsl.2011.02.013>.
- Kulhanek, D.K., Levy, R.H., Clowes, C.D., Prebble, J.G., Rodelli, D., Jovane, L., Morgans, H.E.G., Kraus, C., Zwingmann, H., Griffith, E.M., Scher, H.D., McKay, R.M., and Naish, T.R., 2019, Revised chronostratigraphy of DSDP Site 270 and late Oligocene to early Miocene paleoecology of the Ross Sea sector of Antarctica: Global and Planetary Change, v. 178, p. 46–64, <https://doi.org/10.1016/j.gloplacha.2019.04.002>.
- Kürschner, W.M., Kvaček, Z., and Dilcher, D.L., 2008, The impact of Miocene atmospheric carbon dioxide fluctuations on climate and the evolution of terrestrial ecosystems: Proceedings of the National Academy of Sciences of the United States of America, v. 105, no. 2, p. 449–453, <https://doi.org/10.1073/pnas.0708588105>.
- Kyle, P.R., and Muncy, H.L., 1989, Geology and geochronology of McMurdo Volcanic Group rocks in the vicinity of Lake Morning, McMurdo Sound, Antarctica: Antarctic Science, v. 1, no. 4, p. 345–350, <https://doi.org/10.1017/S0954102089000520>.
- Laskar, J., Robutel, P., Gastineau, M., Correia, A.C.M., and Levrard, B., 2004, A long term numerical solution for the insolation quantities of the Earth: Astronomy & Astrophysics, v. 428, p. 261–285, <https://doi.org/10.1051/0004-6361:20041335>.
- Laskar, J., Fienga, A., Gastineau, M., and Manche, H., 2011, La2010: A new orbital solution for the long-term motion of the Earth: Astronomy & Astrophysics, v. 532, A89, <https://doi.org/10.1051/0004-6361/201116836>.
- Lawson, D.E., 1979, A comparison of the pebble orientations in ice and deposits of the Matanuska Glacier, Alaska: The Journal of Geology, v. 87, no. 6, p. 629–645, <https://doi.org/10.1086/628457>.
- Le Maître, R., Streckeisen, A., Zanettin, B., Le Bas, M., Bonnin, B., Bateman, P., Bellieni, G., Dudek, A., Efremova, S., and Keller, J., 2002, Igneous Rocks. A Classification and Glossary of Terms: Recommendations of the International Union of Geological Sciences Subcommission on the Systematics of Igneous Rocks: New York, Cambridge University Press, 256 p.
- Leutert, T.J., Auderset, A., Martínez-García, A., Modestou, S., and Meckler, A.N., 2020, Coupled Southern Ocean cooling and Antarctic ice sheet expansion during the middle Miocene: Nature Geoscience, v. 13, no. 9, p. 634–639, <https://doi.org/10.1038/s41561-020-0623-0>.
- Levy, R., Harwood, D., Florindo, F., Sangiorgi, F., Tripathi, R., von Eynatten, H., Gasson, E., Kuhn, G., Tripathi, A., DeConto, R., Fielding, C., Field, B., Golledge, N., McKay, R., Naish, T., Olney, M., Pollard, D., Schouten, S., Talarico, F., Warny, S., Willmott, V., Acton, G., Panter, K., Paulsen, T., Taviani, M., and Team, S.S., 2016, Antarctic ice sheet sensitivity to atmospheric CO₂ variations in the early to mid-Miocene: Proceedings of the National Academy of Sciences of the United States of America, v. 113, no. 13, p. 3453–3458, <https://doi.org/10.1073/pnas.1516030113>.
- Levy, R.H., Meyers, S.R., Naish, T.R., Golledge, N.R., McKay, R.M., Crampton, J.S., DeConto, R.M., De Santis, L., Florindo, F., Gasson, E.G.W., Harwood, D.M., Luyendyk, B.P., Powell, R.D., Clowes, C., and Kulhanek, D.K., 2019, Antarctic ice-sheet sensitivity to obliquity forcing enhanced through ocean connections: Nature Geoscience, v. 12, no. 2, p. 132–137, <https://doi.org/10.1038/s41561-018-0284-4>.
- Levy, R.H., Dolan, A.M., Escutia, C., Gasson, E.G.W., McKay, R.M., Naish, T., Patterson, M.O., Pérez, L.F., Shevenell, A.E., van de Flierdt, T., Dickinson, W., Kowalewski, D.E., Meyers, S.R., Ohneiser, C., Sangiorgi, F., Williams, T., Chorley, H.K., Santis, L.D., Florindo, F., Golledge, N.R., Grant, G.R., Halberstadt, A.R.W., Harwood, D.M., Lewis, A.R., Powell, R., and Verret, M., 2022, Chapter 9: Antarctic environmental change and ice sheet evolution through the Miocene to Pliocene—a perspective from the Ross Sea and George V to Wilkes Land Coasts, in Florindo, F., Siegert, M., Santis, L.D., and Naish, T., eds., Antarctic Climate Evolution (2nd Edition): Amsterdam, Elsevier, p. 389–521, <https://doi.org/10.1016/B978-0-12-819109-5.00014-1>.
- Lewis, A.R., and Ashworth, A.C., 2016, An early to middle Miocene record of ice-sheet and landscape evolution from the Friis Hills, Antarctica: Geological Society of America Bulletin, v. 128, p. 719–738, <https://doi.org/10.1130/B31319.1>.
- Lewis, A.R., Marchant, D.R., Kowalewski, D.E., Baldwin, S.L., and Webb, L.E., 2006, The age and origin of the Labyrinth, western Dry Valleys, Antarctica: Evidence for extensive middle Miocene subglacial floods and freshwater discharge to the Southern Ocean: Geology, v. 34, no. 7, p. 513–516, <https://doi.org/10.1130/G22145.1>.
- Lewis, A.R., Marchant, D.R., Ashworth, A.C., Hemming, S.R., and Machlus, M.L., 2007, Major middle Miocene global climate change: Evidence from East Antarctica and the Transantarctic Mountains: Geological Society of America Bulletin, v. 119, p. 11–12, p. 1449–1461, [https://doi.org/10.11130/0016-7606\(2007\)119\[1449:MMMGCC\]2.0.CO;2](https://doi.org/10.11130/0016-7606(2007)119[1449:MMMGCC]2.0.CO;2).
- Lewis, A.R., Marchant, D.R., Ashworth, A.C., Hedenäs, L., Hemming, S.R., Johnson, J.V., Leng, M.J., Machlus, M.L., Newton, A.E., Raine, J.I., Willenbring, J.K., Williams, M., and Wolfe, A.P., 2008, Mid-Miocene cooling and the extinction of tundra in continental Antarctica: Proceedings of the National Academy of Sciences of the United States of America, v. 105, no. 31, p. 10,676–10,680, <https://doi.org/10.1073/pnas.0802501105>.
- Majewski, W., 2010, Planktonic foraminiferal response to middle Miocene cooling in the Southern Ocean (ODP Site 747, Kerguelen Plateau): Acta Palaeontologica Polonica, v. 55, p. 541–560.
- Marchant, D.R., 1993, Miocene glacial stratigraphy and landscape evolution of the western Asgard Range, Antarctica. Vega symposium on the Case for a stable East Antarctic ice sheet, in Marchant, D.R., Denton, G.H., Sugden, D.E., and Swisher III, C.C., Miocene Glacial Stratigraphy and Landscape Evolution of the Western Asgard Range, Antarctica: Geografiska Annaler: Series A, Physical Geography, v. 75, no. 4, p. 303–330, <https://doi.org/10.1080/04353676.1993.11880398>.
- Marschalek, J.W., Zurli, L., Talarico, F., van de Flierdt, T., Vermeech, P., Carter, A., Beny, F., Bout-Roumazeilles, V., Sangiorgi, F., Hemming, S.R., Pérez, L.F., Colleoni, F., Preble, J.G., van Peer, T.E., Perrott, M., Shevenell, A.E., Browne, I., Kulhanek, D.K., Levy, R., Harwood, D., Sullivan, N.B., Meyers, S.R., Griffith, E.M., Hillebrand, C.D., Gasson, E., Siegert, M.J., Keisling, B., Licht, K.J., Kuhn, G., Dodd, J.P., Boshuis, C., De Santis, L., McKay, R.M., Ash, J., Beny, F., Browne, I.M., Cortese, G., De Santis, L., Dodd, J.P., Esper, O.M., Gales, J.A., Harwood, D.M., Ishino, S., Keisling, B.A., Kim, S., Kim, S., Kulhanek, D.K., Laberg, J.S., Leckie, R.M., McKay, R.M., Müller, J., Patterson, M.O., Romans, B.W., Romero, O.E., Sangiorgi, F., Seki, O., Shevenell, A.E., Singh, S.M., Cordeiro de Sousa, I.M., Sugisaki, S.T., van de Flierdt, T., van Peer, T.E., Xiao, W., Xiong, Z., and Expedition, I., 2021, A large West Antarctic Ice Sheet explains early Neogene sea-level amplitude: Nature, v. 600, no. 7889, p. 450–455, <https://doi.org/10.1038/s41586-021-04148-0>.
- Martin, A., Cooper, A., and Dunlap, W.J., 2010, Geochronology of Mount Morning, Antarctica: Two-phase evolution of a long-lived trachyte–basanite–phonolite eruptive center: Bulletin of Volcanology, v. 72, no. 3, p. 357–371, <https://doi.org/10.1007/s00445-009-0319-1>.
- McCabe, C., and Eyles, N., 1988, Sedimentology of an ice-contact glaciomarine delta, Carey Valley, Northern Ireland: Sedimentary Geology, v. 59, no. 1–2, p. 1–14, [https://doi.org/10.1016/0037-0738\(88\)90097-8](https://doi.org/10.1016/0037-0738(88)90097-8).
- McCarroll, D., and Harris, C., 1992, The glaciogenic deposits of Western Llynn, North Wales: Is it terrestrial or marine?: Journal of Quaternary Science, v. 7, no. 1, p. 19–29, <https://doi.org/10.1002/jqs.3390070103>.
- McKay, R., Browne, G., Carter, L., Dunbar, G., Krissek, L., Naish, T., Powell, R., Reed, J., Talarico, F., and Wilch, T., 2009, The stratigraphic signature of the late Cenozoic Antarctic Ice Sheets in the Ross Embayment: Geological Society of America Bulletin, v. 121, no. 11–12, p. 1537–1561, <https://doi.org/10.1130/B26540.1>.
- McKay, R., De Santis, L., Kulhanek, D., and Expedition 374 Scientists, eds., 2019, Ross Sea West Antarctic Ice Sheet History: Proceedings of the International Ocean Discovery Program, v. 374, <https://doi.org/https://doi.org/10.14379/iodp.proc.374.2019>.
- McKay, R., Escutia, C., De Santis, L., Donda, F., Duncan, B., Gohl, K., Gulick, S., Hernández-Molina, J., Hillebrand, C.-D., Hochmuth, K., Kim, S., Kuhn, G., Larner, R., Leitchenkov, G., and Levy, H.R.R., Naish, T., O'Brien, P.F., Pérez, L.E., Shevenell, A., and Williams, T., 2022, Chapter 3—Cenozoic history of Antarctic glaciation and climate from onshore and offshore studies, in Florindo, F., Siegert, M., Santis, L.D., and Naish, T., eds., Antarctic Climate Evolution (2nd edition): Amsterdam, Elsevier, p. 41–164, <https://doi.org/https://doi.org/10.1016/B978-0-12-819109-5.00008-6>.
- Meinshausen, M., Smith, S.J., Calvin, K., Daniel, J.S., Kainuma, M.L.T., Lamarque, J.F., Matsumoto, K., Montzka, S.A., Raper, S.C.B., Riahi, K., Thomson, A., Velders, G.J.M., and Weil, C., 2015, Contribution of greenhouse gas emissions to projected future climate change: Nature Climate Change, v. 5, p. 435–440, <https://doi.org/10.1038/nclimate2627>.

- G.J.M., and Vuuren, D.P.P., 2011, The RCP greenhouse gas concentrations and their extensions from 1765 to 2300: *Climatic Change*, v. 109, no. 1–2, p. 213–241, <https://doi.org/10.1007/s10584-011-0156-z>.
- Menzies, J., 1989, Drumlins—products of controlled or uncontrolled glaciodynamic response?: *Journal of Glaciology*, v. 8, no. 2, p. 151–158.
- Miall, A.D., 1977, Lithofacies types and vertical profile models in braided river deposits: A summary, in Miall, A.D., ed., *Fluvial Sedimentology*: Dallas, Texas, Dallas Geological Society, p. 597–604.
- Miller, J.M., 1989, Glacial advance and retreat sequences in a Permo-Carboniferous section, central Transantarctic Mountains: *Sedimentology*, v. 36, no. 3, p. 419–430, <https://doi.org/10.1111/j.1365-3091.1989.tb00617.x>.
- Naish, T., Powell, R., Levy, R., Wilson, G., Scherer, R., Taralrico, F., Krissek, L., Niessen, F., Pompilio, M., Wilson, T., Carter, L., DeConto, R., Huybers, P., McKay, R., Pollard, D., Ross, J., Winter, D., Barrett, P., Browne, G., Cody, R., Cowan, E., Crampton, J., Dunbar, G., Dunbar, N., Florindo, F., Gebhardt, C., Graham, I., Hannah, M., Hansaraj, D., Harwood, D., Helling, D., Henrys, S., Hinov, L., Kuhn, G., Kyle, P., Laufer, A., Maffioli, P., Magens, D., Mandernack, K., McIntosh, W., Millan, C., Morin, R., Ohneiser, C., Paulsen, T., Persico, D., Raine, I., Reed, J., Riesselman, C., Sagnotti, L., Schmitt, D., Sjuneskog, C., Strong, P., Taviani, M., Vogel, S., Wilch, T., and Williams, T., 2009, Obliquity-paced Pliocene West Antarctic ice sheet oscillations: *Nature*, v. 458, no. 7236, p. 322–328, <https://doi.org/10.1038/nature07867>.
- Nemec, W., 1990, Aspects of sediment movement on steep delta slopes, in Colella, A., and Prior, D.B., eds., *Coarse-Grained Deltas: International Association of Sedimentologists Special Publication 10*, p. 29–73, <https://doi.org/10.1002/9781444303858.ch3>.
- Nemec, W., and Steel, R.J., 1984, Alluvial and coastal conglomerates: Their significant features and some comments on gravelly mass-flow deposits, in Koster, E.H., and Steel, R.J., eds., *Sedimentology of Gravels and Conglomerates: Canadian Society of Petroleum Geologists Memoir 10*, p. 1–31.
- Ohneiser, C., Wilson, G.S., Beltran, C., Dolan, A.M., Hill, D.J., and Prebble, J.G., 2020, Warm fjords and vegetated landscapes in early Pliocene East Antarctica: *Earth and Planetary Science Letters*, v. 534, p. 116045, <https://doi.org/10.1016/j.epsl.2019.116045>.
- Passchier, S., Browne, G., Field, B., Fielding, C.R., Krissek, L.A., Panter, K., Pekar, S.F., and ANDRILL-SMS Science Team, 2011, Early and middle Miocene Antarctic glacial history from the sedimentary facies distribution in the AND-2A drill hole, Ross Sea, Antarctica: *Geological Society of America Bulletin*, v. 123, p. 2352–2365, <https://doi.org/10.1130/B30334.1>.
- Patterson, M.O., McKay, R., Naish, T., Escutia, C., Jimenez-Espejo, F.J., Raymo, M.E., Meyers, S.R., Tauxe, L., Brinkhuis, H., and IODP Expedition 318 Scientists, 2014, Orbital forcing of the East Antarctic ice sheet during the Pliocene and Early Pleistocene: *Nature Geoscience*, v. 7, no. 11, p. 841–847, <https://doi.org/10.1038/ngeo2273>.
- Pérez, L.F., De Santis, L., McKay, R.M., Larer, R.D., Ash, J., Bart, P.J., Böhm, G., Brancatelli, G., Browne, G., Colleoni, F., Dodd, J.P., Geletti, R., Harwood, D.M., Kuhn, G., Laberg, J.S., Leckie, R.M., Levy, R.H., Marschalek, J., Mateo, Z., Naish, T.M., Sangiorgi, F., Shevenell, A., Sorlien, C.C., van de Flierdt, T., and IODP Expedition 374 Scientists, 2021, Early and middle Miocene ice sheet dynamics in the Ross Sea: Results from integrated core-log-seismic interpretation: *Geological Society of America Bulletin*, v. 134, p. 348–370, <https://doi.org/10.1130/B35814.1>.
- Pierce, E.L., van de Flierdt, T., Williams, T., Hemming, S.R., Cook, C.P., and Passchier, S., 2017, Evidence for a dynamic East Antarctic ice sheet during the mid-Miocene climate transition: *Earth and Planetary Science Letters*, v. 478, Supplement C, p. 1–13, <https://doi.org/10.1016/j.epsl.2017.08.011>.
- Pinseel, E., Vijver, B.V.d., Wolfe, A.P., Harper, M., Antonides, D., Ashworth, A.C., Ector, L., Lewis, A.R., Perren, B., Hodgson, D.A., Sabbe, K., Verleyen, E., and Vyverman, W., 2021, Extinction of austral diatoms in response to large-scale climate dynamics in Antarctica: *Science Advances*, v. 7, <https://doi.org/10.1126/sciadv.abb3233>.
- Plint, A.G., 1988, Sharp-based shoreface sequences and “offshore bars” in the Cardium Formation of Alberta: Their relationship to relative changes in sea level, in Wilgus, C.K., Hastings, B.S., Ross, C.A., Posamentier, H., Van Wagoner, J.C., and Kendall, C.G.S.C., eds., *Sea-level Changes: An Integrated Approach: Society of Economic Paleontologists and Mineralogists Special Publication 42*, p. 357–370.
- Porter, S.C., and Beget, J.E., 1981, Provenance and Depositional Environments of Late Cenozoic Sediments in Permafrost Cores from Lower Taylor Valley, Antarctica: Washington, D.C., American Geophysical Union, Antarctic Research Series, v. 33, 465 p., <https://doi.org/10.1029/AR033p0351>.
- Postma, G., 1986, Classification for sediment gravity-flow deposits based on flow conditions during sedimentation: *Geology*, v. 14, no. 4, p. 291–294, [https://doi.org/10.1130/0091-7613\(1986\)14<291:CFSGDB>2.0.CO;2](https://doi.org/10.1130/0091-7613(1986)14<291:CFSGDB>2.0.CO;2).
- Prebble, J.G., Raine, J.I., Barrett, P.J., and Hannah, M.J., 2006, Vegetation and climate from two Oligocene glacioeustatic sedimentary cycles (31 and 24 Ma) cored by the Cape Roberts Project, Victoria Land Basin, Antarctica: *Palaeogeography, Palaeoclimatology, Palaeoecology*, v. 231, no. 1, p. 41–57, <https://doi.org/10.1016/j.palaeo.2005.07.025>.
- Prentice, M., Bockheim, J.G., Wilson, S.C., Burkle, L.H., Hodell, D.A., Schlüchter, C., and Kellogg, D.E., 1993, Late Neogene Antarctic glacial history: evidence from central Wright Valley: *The Antarctic Paleoenvironment: A Perspective on Global Change: Part Two*, v. 60, p. 207–250, <https://doi.org/10.1002/9781118668061.ch11>.
- Raffi, I., Wade, B.S., Pálike, H., Beu, A.G., Cooper, R., Crundwell, M.P., Krijgsman, W., Moore, T., Raine, I., Sardella, R., and Vernyhorova, Y.V., 2020, Chapter 29: The Neogene period, in Gradstein, F.M., Ogg, J.G., Schmitz, M.D., and Ogg, G.M., eds., *Geologic Time Scale 2020*: Amsterdam, Elsevier, p. 1141–1215, <https://doi.org/10.1016/B978-0-12-824360-2.00029-2>.
- Raitzsch, M., Bijma, J., Bickert, T., Schulz, M., Holbourn, A., and Kučera, M., 2021, Atmospheric carbon dioxide variations across the middle Miocene climate transition: *Climate of the Past*, v. 17, no. 2, p. 703–719, <https://doi.org/10.5194/cp-17-703-2021>.
- Retallack, G.J., 2009, Refining a pedogenic-carbonate CO₂ paleobarometer to quantify a middle Miocene greenhouse spike: *Palaeogeography, Palaeoclimatology, Palaeoecology*, v. 281, no. 1, p. 57–65, <https://doi.org/10.1016/j.palaeo.2009.07.011>.
- Rimet, F., Feret, L., Bouchez, A., Dorioz, J.-M., and Dambrine, E., 2019, Factors influencing the heterogeneity of benthic diatom communities along the shoreline of natural alpine lakes: *Hydrobiologia*, v. 839, no. 1, p. 103–118, <https://doi.org/10.1007/s10750-019-03999-z>.
- Sangiorgi, F., Bijl, P.K., Passchier, S., Salzmann, U., Schouten, S., McKay, R., Cody, R.D., Pross, J., van de Flierdt, T., Bohaty, S.M., Levy, R., Williams, T., Escutia, C., and Brinkhuis, H., 2018, Southern Ocean warming and Wilkes Land ice sheet retreat during the mid-Miocene: *Nature Communications*, v. 9, no. 1, p. 317, <https://doi.org/10.1038/s41467-017-02609-7>.
- Scher, H.D., Bohaty, S.M., Zachos, J.C., and Delaney, M.L., 2011, Two-stepping into the icehouse: East Antarctic weathering during progressive ice-sheet expansion at the Eocene–Oligocene transition: *Geology*, v. 39, no. 4, p. 383–386, <https://doi.org/10.1130/G31726.1>.
- Shanmugam, G., 1996, High-density turbidity currents: are they sandy debris flows?: *Journal of Sedimentary Research*, v. 66, no. 1, p. 2–10, <https://doi.org/10.1306/D42682E-2B26-11D7-8648000102C1865D>.
- Shevenell, A.E., Kennett, J.P., and Lea, D.W., 2004, Middle Miocene Southern Ocean cooling and Antarctic cryosphere expansion: *Science*, v. 305, no. 5691, p. 1766–1770, <https://doi.org/10.1126/science.1100061>.
- Shevenell, A.E., Kennett, J.P., and Lea, D.W., 2008, Middle Miocene ice sheet dynamics, deep-sea temperatures, and carbon cycling: A Southern Ocean perspective: *Geochemistry, Geophysics, Geosystems*, v. 9, no. 2, Q02006, <https://doi.org/10.1029/2007GC001736>.
- Sosdian, S.M., Greenop, R., Hain, M.P., Foster, G.L., Pearson, P.N., and Lear, C.H., 2018, Constraining the evolution of Neogene ocean carbonate chemistry using the boron isotope pH proxy: *Earth and Planetary Science Letters*, v. 498, p. 362–376, <https://doi.org/10.1016/j.epsl.2018.06.017>.
- Spector, P., and Balco, G., 2021, Exposure-age data from across Antarctica reveal mid-Miocene establishment of polar desert climate: *Geology*, v. 49, no. 1, p. 91–95, <https://doi.org/10.1130/G47783.1>.
- Steinhorstottir, M., Jardine, P.E., and Rember, W.C., 2021, Near-future pCO₂ during the hot Miocene climatic optimum: *Paleoceanography and Paleoclimatology*, v. 36, <https://doi.org/10.1029/2020PA003900>.
- Sugden, D., and Denton, G., 2004, Cenozoic landscape evolution of the Convoy Range to Mackay Glacier area, Transantarctic Mountains: onshore to offshore synthesis: *Geological Society of America Bulletin*, v. 116, no. 7–8, p. 840–857, <https://doi.org/10.1130/B25356.1>.
- Sugden, D.E., Marchant, D.R., and Denton, G.H., 1993, The case for a stable East Antarctic Ice Sheet: *Geografiska Annaler*, v. 75, p. 151–154, <https://doi.org/10.1080/04353676.1993.11880392>.
- Sugden, D.E., Denton, G.H., and Marchant, D.R., 1995, Landscape evolution of the Dry Valleys, Transantarctic Mountains: Tectonic implications: *Journal of Geophysical Research: Solid Earth*, v. 100, no. B6, p. 9949–9967, <https://doi.org/10.1029/94JB02875>.
- Super, J.R., Thomas, E., Pagan, M., Huber, M., O'Brien, C., and Hull, P.M., 2018, North Atlantic temperature and pCO₂ coupling in the early–middle Miocene: *Geology*, v. 46, no. 6, p. 519–522, <https://doi.org/10.1130/G40228.1>.
- Tebaldi, C., Debeire, K., Eyring, V., Fischer, E., Fyfe, J., Friedlingstein, P., Knutti, R., Lowe, J., O'Neill, B., Sanderson, B., van Vuuren, D., Riahi, K., Meinshausen, M., Nicholls, Z., Tokarska, K.B., Hurtt, G., Kriegler, E., Lamarche, J.F., Meehl, G., Moss, R., Bauer, S.E., Boucher, O., Brovkin, V., Byun, Y.H., Dix, M., Gualdi, S., Guo, H., John, J.G., Kharin, S., Kim, Y., Koshiro, T., Ma, L., Olivie, D., Panikkar, S., Qiao, F., Rong, X., Rosenbloom, N., Schupfner, M., Séférian, R., Sellier, A., Semmler, T., Shi, X., Song, Z., Steger, C., Stouffer, R., Swart, N., Tachiiri, K., Tang, Q., Tabe, H., Volodin, E., Wyser, K., Xin, X., Yang, S., Yu, Y., and Ziehn, T., 2021, Climate model projections from the Scenario Model Intercomparison Project (ScenarioMIP) of CMIP6: Earth System Dynamics: *ESD*, v. 12, no. 1, p. 253–293, <https://doi.org/10.5194/esd-12-253-2021>.
- Thomas, G.S., Chiverrell, R.C., and Huddart, D., 2004, Ice-marginal depositional responses to readvance episodes in the Late Devensian deglaciation of the Isle of Man: *Quaternary Science Reviews*, v. 23, no. 1–2, p. 85–106, <https://doi.org/10.1016/j.quascirev.2003.10.012>.
- Tye, R.S., and Coleman, J.M., 1989, Depositional processes and stratigraphy of fluvially dominated lacustrine deltas: Mississippi delta plain: *Journal of Sedimentary Research*, v. 59, no. 6, p. 973–996.
- Utescher, T., Bruch, A.A., Micheels, A., Mosbrugger, V., and Popova, S., 2011, Cenozoic climate gradients in Eurasia—a palaeo-perspective on future climate change?: *Palaeogeography, Palaeoclimatology, Palaeoecology*, v. 304, no. 3–4, p. 351–358, <https://doi.org/10.1016/j.palaeo.2010.09.031>.
- Valletta, R.D., Willenbring, J.K., Lewis, A.R., Ashworth, A.C., and Caffee, M., 2015, Extreme decay of meteoric beryllium-10 as a proxy for persistent aridity: *Scientific Reports*, v. 5, <https://doi.org/10.1038/srep17813>.
- van der Meer, J.J.M., 1993, Microscopic evidence of subglacial deformation: *Quaternary Science Reviews*, v. 12, p. 553–587, [https://doi.org/10.1016/0277-3791\(93\)90069-X](https://doi.org/10.1016/0277-3791(93)90069-X).
- van der Meer, J.J., and Menzies, J., 2011, The micromorphology of unconsolidated sediments: *Sedimentary Geology*, v. 238, no. 3–4, p. 213–232, <https://doi.org/10.1016/j.sedgeo.2011.04.013>.
- van der Meer, J., Menzies, J., and Rose, J., 2003, Subglacial Till: The Deforming Glacier Bed: *Quaternary Science Reviews*, v. 22, p. 1659–1685, [https://doi.org/10.1016/S0277-3791\(03\)00141-0](https://doi.org/10.1016/S0277-3791(03)00141-0).
- Verducci, M., Foresi, L.M., Scott, G.H., Sprovieri, M., Lirer, F., and Pelosi, N., 2009, The Middle Miocene climatic transition in the Southern Ocean: Evidence of

- paleoclimatic and hydrographic changes at Kerguelen plateau from planktonic foraminifers and stable isotopes: Palaeogeography, Palaeoclimatology, Palaeoecology, v. 280, p. 371–386, <https://doi.org/10.1016/j.palaeo.2009.06.024>.
- Vlastélic, I., Carpentier, M., and Lewin, É., 2005, Miocene climate change recorded in the chemical and isotopic (Pb , Nd , Hf) signature of Southern Ocean sediments: Geochemistry, Geophysics, Geosystems, v. 6, <https://doi.org/10.1029/2004GC000819>.
- Walker, R.G., and James, N.P., 1992, Facies Models: Response to Sea Level Change: St. Johns, Newfoundland, Geological Association of Canada, 409 p.
- Warny, S., Askin, R.A., Hannah, M.J., Mohr, B.A.R., Raine, J.I., Harwood, D.M., Florindo, F., and the SMS Science Team, 2009, Palynomorphs from a sediment core reveal a sudden remarkably warm Antarctica during the middle Miocene: *Geology*, v. 37, no. 10, p. 955–958, <https://doi.org/10.1130/G30139A.1>.
- Westerhold, T., Marwan, N., Drury, A.J., Liebrandt, D., Agnini, C., Anagnostou, E., Barnet, J.S.K., Bohaty, S.M., De Vleeschouwer, D., Florindo, F., Frederichs, T., Hodell, D.A., Holbourn, A.E., Kroon, D., Lauretano, V., Littler, K., Lourens, L.J., Lyle, M., Pälike, H., Röhl, U., Tian, J., Wilkens, R.H., Wilson, P.A., and Zachos, J.C., 2020, An astronomically dated record of Earth's climate and its predictability over the last 66 million years: *Science*, v. 369, no. 6509, p. 1383–1387, <https://doi.org/10.1126/science.aba6853>.
- Wilson, G.S., Levy, R.H., Naish, T.R., Powell, R.D., Flordino, F., Ohneiser, C., Sagnotti, L., Winter, D.M., Cody, R., Henrys, S., Ross, J., Krissek, L., Nissen, F., Pompilio, M., Scherer, R., Alloway, B.V., Barrett, P.J., Brachfeld, S., Browne, G., Carter, L., Cowan, E., Crampton, J., DeConto, R.M., Dunbar, G., Dunbar, N., Dunbar, R., von Eynatten, H., Gebhardt, C., Giorgetti, G., Graham, I., Hannah, M., Hansaraj, D., Harwood, D.M., Hinov, L., Jarrard, R.D., Joseph, L., Kominz, M., Kuhn, G., Kyle, P., Läufer, A., McIntosh, W.C., McKay, R., Maffioli, P., Magens, D., Millan, C., Monien, D., Morin, R., Paulsen, T., Persico, D., Pollard, D., Raine, J.I., Riesselman, C., Sandroni, S., Schmitt, D., Sjuneskog, C., Strong, C.P., Talarico, F., Taviani, M., Villa, G., Vogel, S., Wilch, T., Williams, T., Wilson, T.J., and Wise, S., 2012, Neogene tectonic and climatic evolution of the Western Ross Sea, Antarctica—Chronology of events from the AND-1B drill hole: *Global and Planetary Change*, v. 96–97, p. 189–203, <https://doi.org/10.1016/j.gloplacha.2012.05.019>.
- Witkowski, C.R., Weijers, J.W.H., Blais, B., Schouten, S., and Sinninghe Damsté, J.S., 2018, Molecular fossils from phytoplankton reveal secular PCO_2 trend over the Phanerozoic: *Science Advances*, v. 4, no. 11, <https://doi.org/10.1126/sciadv.aat4556>.
- Wolfe, A.P., 1994, Late Wisconsinan and Holocene diatom stratigraphy from Amarok Lake, Baffin Island, NWT, Canada: *Journal of Paleolimnology*, v. 10, no. 2, p. 129–139, <https://doi.org/10.1007/BF00682509>.
- You, Y., 2010, Climate-model evaluation of the contribution of sea-surface temperature and carbon dioxide to the Middle Miocene Climate Optimum as a possible analogue of future climate change: *Australian Journal of Earth Sciences: An International Geoscience Journal of the Geological Society of Australia*, v. 57, no. 2, p. 207–219, <https://doi.org/10.1080/08120090903521671>.
- You, Y., Huber, M., Müller, R.D., Poulsen, C.J., and Ribbe, J., 2009, Simulation of the middle Miocene climate optimum: *Geophysical Research Letters*, v. 36, p. 1–5, <https://doi.org/10.1029/2008GL036571>.
- Zachos, J., Pagani, M., Sloan, L., Thomas, E., and Billups, K., 2001, Trends, rhythms, and aberrations in global climate 65 Ma to present: *Science*, v. 292, no. 5517, p. 686–693, <https://doi.org/10.1126/science.1059412>.
- Zhang, Y.G., Pagani, M., Liu, Z., Bohaty, S.M., and DeConto, R., 2013, A 40-million-year history of atmospheric CO_2 : *Philosophical Transactions of the Royal Society A: Mathematical, Physical and Engineering Sciences*, v. 371, no. 2001, <https://doi.org/10.1098/rsta.2013.0096>.

SCIENCE EDITOR: BRAD S. SINGER

ASSOCIATE EDITOR: SHASTA MARRERO

MANUSCRIPT RECEIVED 28 MARCH 2022

MANUSCRIPT ACCEPTED 5 JULY 2022

Printed in the USA